Chapter 4
Image Re-processing of Satellite Imageries

In this chapter, the focus is re-processing satellite imageries. Satellite imagery are images of Earth or other planets collected by Imaging satellites. The quality of satellite imagery is judged by its resolution. The resolution associated to satellite imagery are namely spatial, spectral, temporal, geometric and radiometric (Campbell 2002). The spatial resolution is the pixel size of an image that represents the size of the surface area. Spectral resolution is the discrete segmentation of the electromagnetic spectrum that describes the number of intervals and interval size of the sensor wavelength. Temporal resolution describes the time-duration between imagery collection periods for a given surface location. Geometric resolution describes the ability of the satellite sensors to effectively image a portion of the Earth's surface in a single pixel. Radiometric resolution describes the ability of imaging system to record many levels of brightness in bit-depths of 8-bit (0–255), 11-bit (0–2047), 12-bit (0–4095) or 16-bit (0–65,535).

The quality of the resolution depends on the satellite view and the imaging camera. For example, 'Landsat 7' 15 m satellite imagery is not as sharp as either the 'Spot' 10 m or 'IRS-1C' 5 m satellite imagery but it has large area coverage (Landinfo 2018). GeoEye-1 has an orbit altitude of about 770 km/478 Miles and is capable of producing imagery with a ground sampling distance of 46 cm, meaning it can detect objects of that diameter or greater (GeoEye 2018). NASA (2015) revealed the high-tech of the Earth Polychromatic Imaging Camera (EPIC) used for Deep Space Climate Observatory (DSCOVR) satellite. EPIC takes a series of 10 images using different narrowband filters from ultraviolet to near infrared to produce a variety of science products. One of the novel features of EPIC is that it has a very fast image processing time.

In this chapter, the satellite imagery that was re-processed is the GES-DISC Interactive Online Visualization ANd aNalysis Infrastructure (Giovanni). Giovanni users have access to satellite imagery from multiple remote sites. Its image processing platform supports multiple data formats namely Hierarchical Data Format (HDF), HDF-EOS, network Common Data Form (netCDF), GRIdded Binary (GRIB), GIF, and binary. Also, Giovanni have multiple plot types e.g. area, time, Hovmoller, and

M. E. Emetere, *Environmental Modeling Using Satellite Imaging and Dataset Re-processing*, Studies in Big Data 54,
https://doi.org/10.1007/978-3-030-13405-1_4

image animation. Giovanni users have free-access to data on atmospheric chemistry, atmospheric temperature, water vapor and clouds, atmospheric aerosols, precipitation, ocean chlorophyll and surface temperature (Acker and Leptoukh 2007). Its primary satellite imagery consists of global gridded data sets with reduced spatial resolution. It is based upon this fact, the need to re-process the satellite imagery using open source software (CERN-ROOT) and library (OpenCV C++) was borne. This gesture is meant to unravel deeper information of dataset through the adoption of modern computational techniques.

4.1 Image Processing

The satellite imagery that was used covers West Africa and some few countries around it. The scope of the satellite imagery is aerosols optical depth for January–December, 2007 and January–December, 2013. The raw satellite image was converted from '.gif' to 'png' to ensure an enhanced image. The image properties of the raw satellite data and the converted data are shown in Table 4.1. It is observed that the new images are better based on the dpi (Dots Per Inch) width, dpi height, sample per pixel, pixel width and pixel height.

The raw satellite image of aerosol optical depth pixel count is shown in Fig. 4.1.

The pixel of Fig. 4.1 was re-processed in 8 bits image. The y-pixel was potted against the x-pixel to obtain the original image in another format whose information is inverse to the original satellite imagery (Fig. 4.1). In Fig. 4.1, the AOD pixel counts is highest at the south of Chad, Senegal and Mali; north of Cameroun, Benin, Togo, Ghana, Cote d'Ivoire, Sierra Leone, Gambia; north-central of Nigeria and Guinea.

The redefinition of the satellite image shows the following

Table 4.1 Image properties

Number	Parameters	Old image	New image
1	pixelWidth	700	1242
2	pixelHeight	500	646
3	typeIdentifier	com.compuserve.gif	public.png
4	format	gif	png
5	dpiWidth	72,000	144,000
6	dpiHeight	72,000	144,000
7	samplesPerPixel	3	4
8	bitsPerSample	8	8
9	hasAlpha	no	yes
10	space	RGB	RGB
11	profile	sRGB IEC61966-2.1	Color LCD

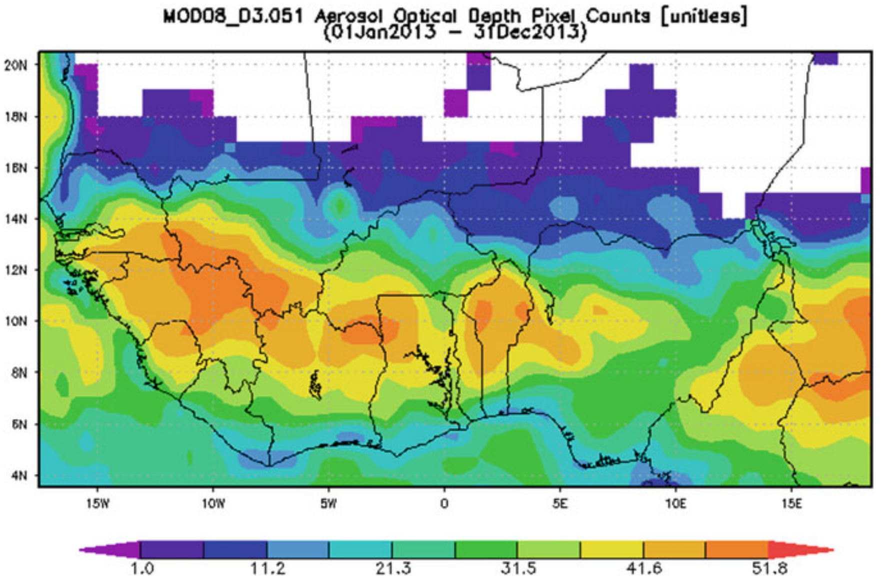

Fig. 4.1 Satellite image AOD pixel counts-Jan. to Dec., 2013

i. The inactive part (white region) of Fig. 4.1 was reconstructed Fig. 4.2.
ii. A clear spot in the north-central of Nigeria that may typify a special feature that require more investigation.
iii. Evidence of massive aerosol retention across latitude 7°–13°N which queries the authenticity of the major wind that affect West Africa region between latitudes 9° and 20°N (Rafferty 2010).
iv. The wind dynamics i.e. southwesterly that blows during warmer months and northeasterly that blows during cooler months have low impact on aerosols distribution within latitude 7°–13°N.
v. There is a significant aerosol path (red lines) that continuously connects from land to sea and vice versa.

The contour detection algorithm was used to determine contours not visible to the eye. The circles are used to measure the width of the contour i.e. the diameter of the circle. The blue arrow shows the insignificant circle because the contour inside the circle is a regional boundary. The red arrow shows the relevant circle which contains contours that cannot be spotted by the human eye (Fig. 4.3). 40% of the circles actually points to the useful contours while about 60% only relates to boundary lines. The sizes of the circle can be measured and the given locations within the circle can be investigated for more information.

The 3D image (Fig. 4.4) shows the relation between the derived matrix of the image. The 70–150 pixel (along Y-axis) corresponds to locations under intense influence of the Sahara dust. The 0–50 pixels (along Y-axis) show locations on Fig. 4.1 that have mechanisms for dousing the influence of Sahara dust via wind convection

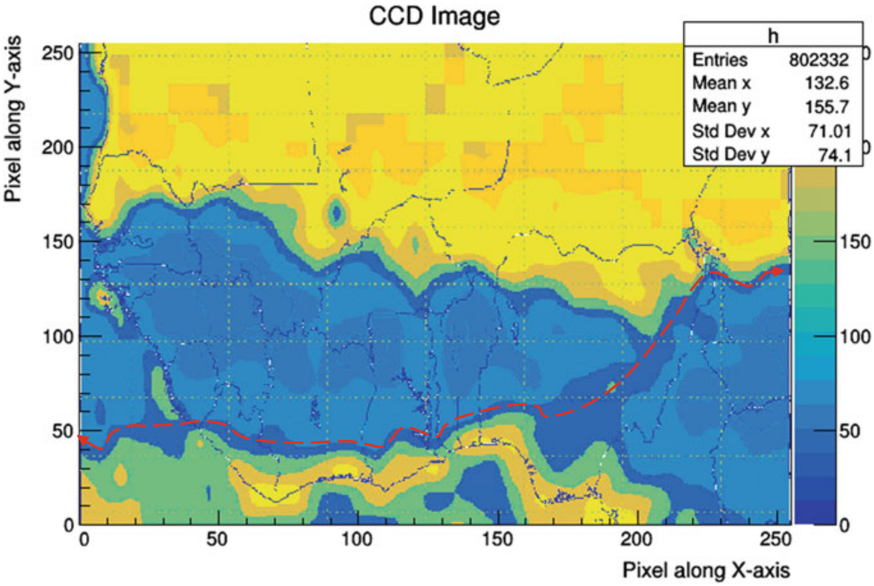

Fig. 4.2 x and y pixel redefinition of the satellite image

Fig. 4.3 Contour detection of satellite image

or rainfall patterns (Emetere et al. 2017a, b; Emetere 2017). One of the importance of Fig. 4.4is the characterization of the vertical profile. For example, within 0–70 pixel, the vertical or z-axis of Fig. 4.4 show that at the lower troposphere, there may be high aerosol particulates. Hence, the background aerosol content (BAC) over a region maybe known. While some location between latitude 14° and 20°N have decreased aerosol particulates as it disperses from the troposphere into the stratosphere, loca-

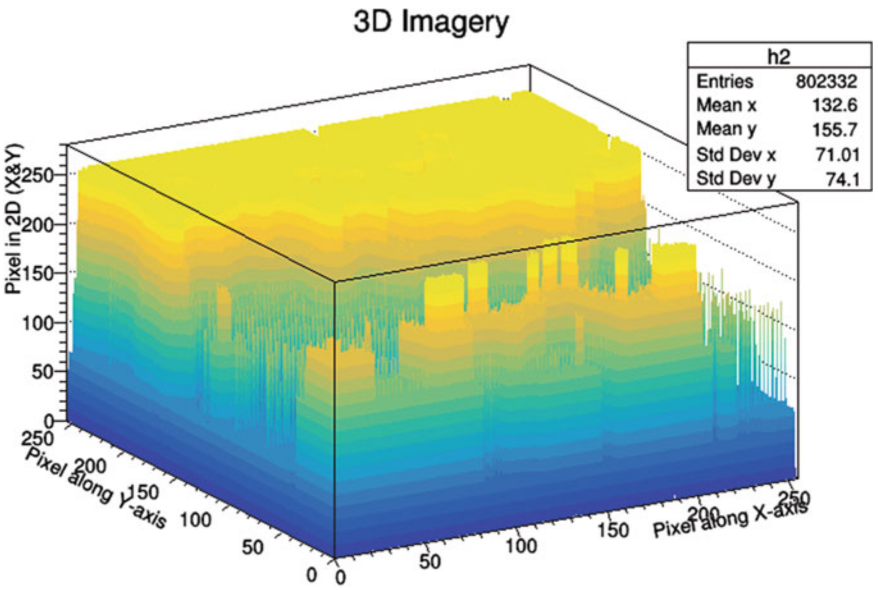

Fig. 4.4 3D setting of satellite image

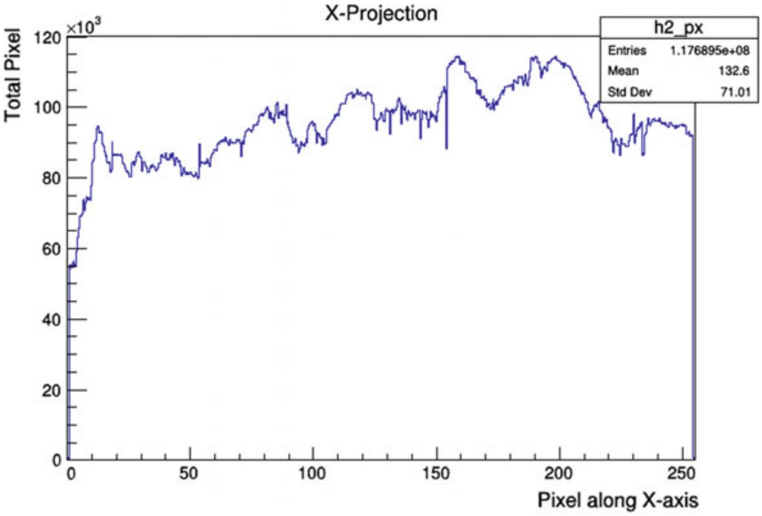

Fig. 4.5 X-projection of satellite image

tions between latitude 7° and 13°N have increased aerosol particulates as it disperses from the troposphere into the stratosphere.

Figure 4.5 show the projection along the x axis of Fig. 4.1. Projection along x or y takes its root from the mathematical Eq. (4.1) below:

$$\vec{X}_k^h(s) = \begin{pmatrix} \vec{X}_k^0 \\ 1 \end{pmatrix} + s \begin{pmatrix} \vec{t} \\ 0 \end{pmatrix} \tag{4.1}$$

here $\vec{t}$ is tangent direction, s is the free parameter for points along the line, $\vec{X}_k^0$ is the arbitrary points on the image coordinates, and $\vec{X}_k^h(s)$ is the parallel lines in the image coordinates.

Normally, the projection along an image axis should be represented by parallel lines, however, there are situation of distortions due to the properties of the image. Hence, a parallel line may be reconstructed as a Gaussian line or multiple sinusoidal line. Image projection along axes can be influenced by the intrinsic and extrinsic calibration of the camera, feature of the image (i.e. radiometry, reflection and colour), digital image formation, and image noise. Image reconstruction of the projection may be influenced by the algebraic nature of the parallel line (Eq. 4.2), frequency domain (Eq. 4.3) and filtered back projection (Eq. 4.4).

$$p_m = \sum_{n=1}^{N} w_{m,n} f_n = w_m f \tag{4.2}$$

$w_{m,n}$ is the weight, p_m is the stripe sum, and f_n is the vector of the 'n' unknown image-pixel.

$$F(u, v) = \int_{-\infty}^{\infty} \int_{-\infty}^{\infty} f(x, y) \exp \mathrm{j}(ux + vy) dx dy \tag{4.3}$$

$F(u, v)$ is the 2D image spectrum, $f(x, y)$ is the image pixel in the x and y axes, u and v are the positions in the x and y axes respectively.

$$b(x, y) = \int_{0}^{\pi} P_\theta(\tau) d\theta \tag{4.4}$$

$b(x, y)$ is the back-projection operator, τ is the discretization of projections, P_θ angle dependent stripe sum. The type of image projection discussed here is the filtered-back projection.

The projection along the x axis relates to the x-component of the satellite image in magnitude of pixels along the x-axis of Fig. 4.1. For example, on the pixel 150 and 200, the x-component of the total pixels is highest over Nigeria, Chad etc. Also, two points (165 and 190) was maximum which clearly shows that there are higher aerosols dispersion along these points. Another way of describing or reporting projections along either x or y axis, is by the number, shape and magnitude of clear peaks. The peaks in Fig. 4.5 are on the pixel-10 (Gambia and Senegal), pixel-85 (Cote d'Ivoire and southern Mali), pixel-120 (Ghana and Burkina Faso), pixel-160 (Nigeria) and pixel-200 (Nigeria and northern Cameroun).

Also, considering the Y-Projection of Fig. 4.1 i.e. the magnitude of pixels along the y-axis, it can be observed that the pixel reaches its peak values above 170,000 and

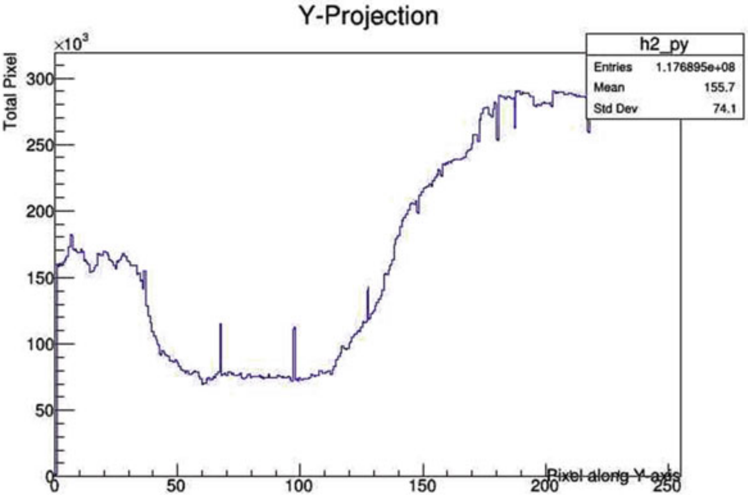

Fig. 4.6 Y-projection of satellite image

290,000. The peak was found at >40 pixel (southern parts of Liberia, Cote d'Ivoire, Ghana, Togo, Benin and Nigeria) and >180 pixel (Mauritania, Mali and Niger). From Fig. 4.1, the region where the peak is found have low aerosol count pixel. The two minor peaks found at the trough of the shape i.e. Fig. 4.6 are at pixel-68 (northern Sierra Leone, northern Liberia, southern Guinea, southern Ghana, southern Togo, southern Benin, central Nigeria and northern Cameroun) and pixel-99 (central Guinea, northern Cote d'Ivoire, northern Ghana, northern Togo, northern Benin and Central Nigeria).

The spectrum analysis of the satellite image (Fig. 4.1) is shown in Fig. 4.7. The spectrum analysis shows the vertical profile and turbulence of aerosols. The aerosols activities i.e. dispersion, distribution and loading are illustrated by the color-mix represented. For example, within 30–110 pixel on the x-axis arrow shows region of highest aerosol count pixel-mostly due to Sahara dust and anthropogenic pollution in the given locations. The vertical profiles (as seen on the z-axis) show that aerosol forms layers within the atmosphere. The blue cross-sectional area shows region of low aerosol distribution.

Aerosol extinction optical depth at 388 nm was obtained from OMI/Aura level-2 near UV Aerosol data product (OMAERUV). OMAERUV measures aerosols in five atmospheric levels namely, Aerosol Layer Height (ALH), Normalized Radiance (NR), Lambert equivalent Reflectivity (LER), Surface Albedo (SA), and Imaginary Component of Refractive Index (ICRI). Aerosol Extinction optical depth is a measure of the annihilation of the solar beam by dust and haze.

In Fig. 4.8, the high AEOD can be found both on land (Niger, Chad, Mali, Mauritania and fragment-parts in southern Nigeria) and sea (coastal part of West Africa). The high values in Niger, Chad, Mali and Mauritania is due to the Sahara dust (Lindén

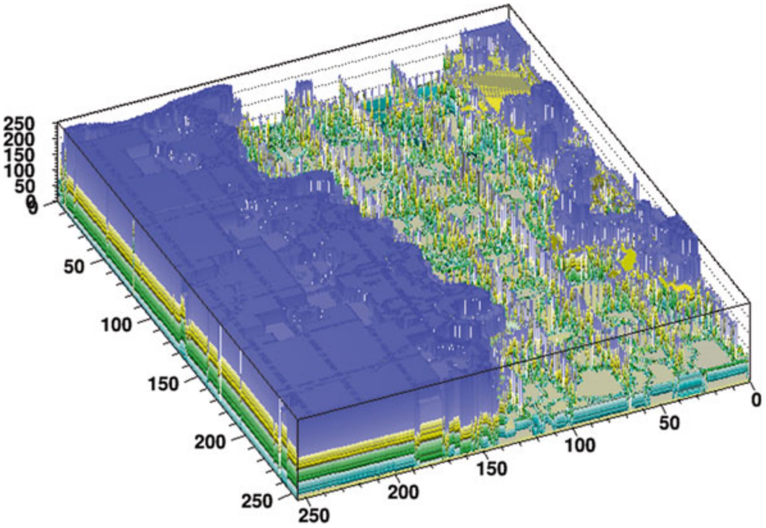

Fig. 4.7 The spectrum analysis of the satellite image

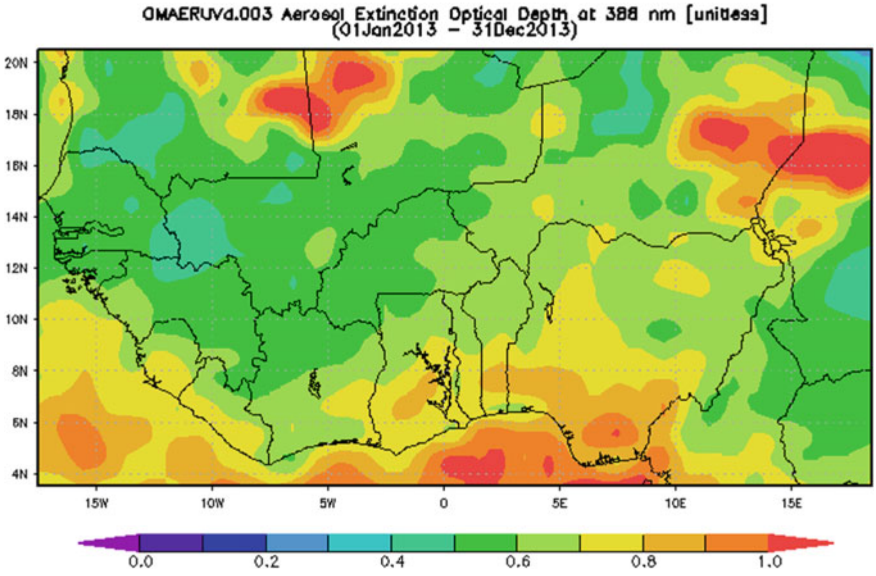

Fig. 4.8 Satellite image AEOD at 388 nm, Jan. to Dec., 2013

et al. 2012). The high value of AEOD at the fragment-parts in southern Nigeria is due to gas flaring (Omotosho et al. 2015).

Recall that it was acknowledged that the colour bar in Fig. 4.2 was inversely proportional to the satellite image. In like manner it was observed that Fig. 4.9

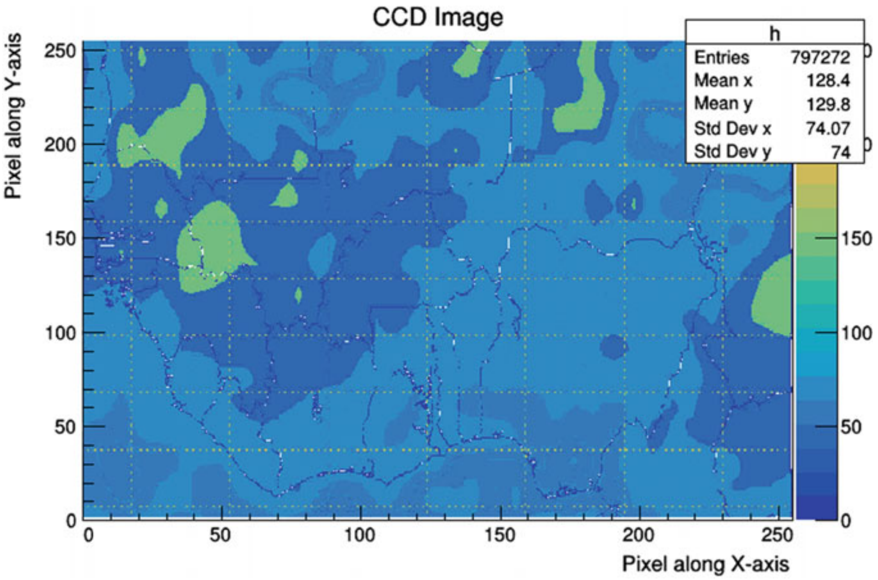

Fig. 4.9 x and y pixel redefinition of the satellite image

contradicts the satellite image in Fig. 4.8. The dark blue patches depict the highest AEOD which was not the case in Fig. 4.9. The affected areas were central Nigeria, northern Ghana, northern Cote d'Ivoire, Burkina Faso, Mali, Mauritania, Senegal, Gambia, Guinea and northern Sierra Leone. The validation of this site has been reported (Emetere 2016a, b; Emetere et al. 2017a, b, c; Emetere and Akinyemi 2017). The most interesting part of the image processing is that it shows the highest and lowest colour representation of the aerosol properties investigated.

Figure 4.10 show the circles surrounding some interesting features that cannot be seen in Figs. 4.8 and 4.9. For example, the biggest circle over Nigeria show region that have been confirmed by several research to have intense air pollution due to gas flaring (Emetere et al. 2015a, b; Omotosho et al. 2017). All the big circles show similar deductions that would be substantiated in the next chapter.

Figure 4.11 the scanty AEOD distribution at the surface of the 3D image show that the dust and haze contributes significantly in the aerosol content over the study area. In other words, the percentage of dust and haze can be roughly estimated using a well-planned computational technique. In this case, the author suggests 36%. The implication of this observation is that the anthropogenic pollution is the major contributor to aerosol distribution over West Africa. It can be observed that the background aerosol content (mainly dust and haze is high). However, some region (the sea at the coastal) demonstrated zero background aerosol content (Fig. 4.11). This means that the high haze level (Fig. 4.8) were not from ship activities at the coastal. Hence the haze was basically transport from the land. The 3D image also

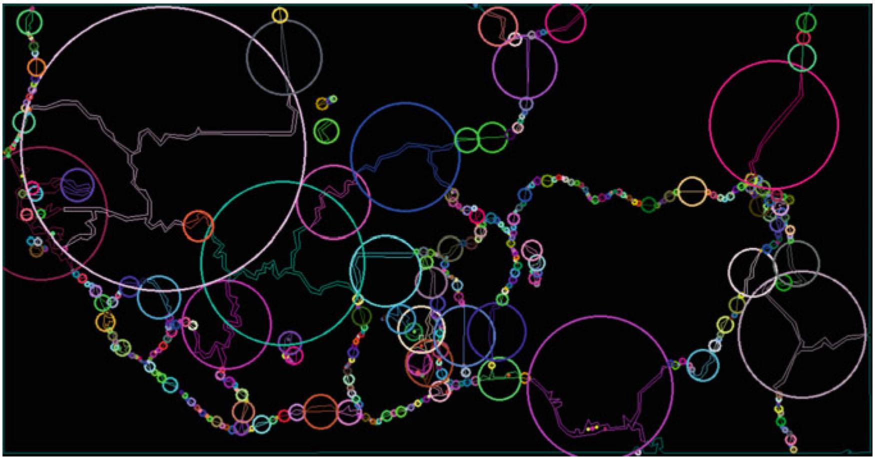

Fig. 4.10 Contour detection of satellite image

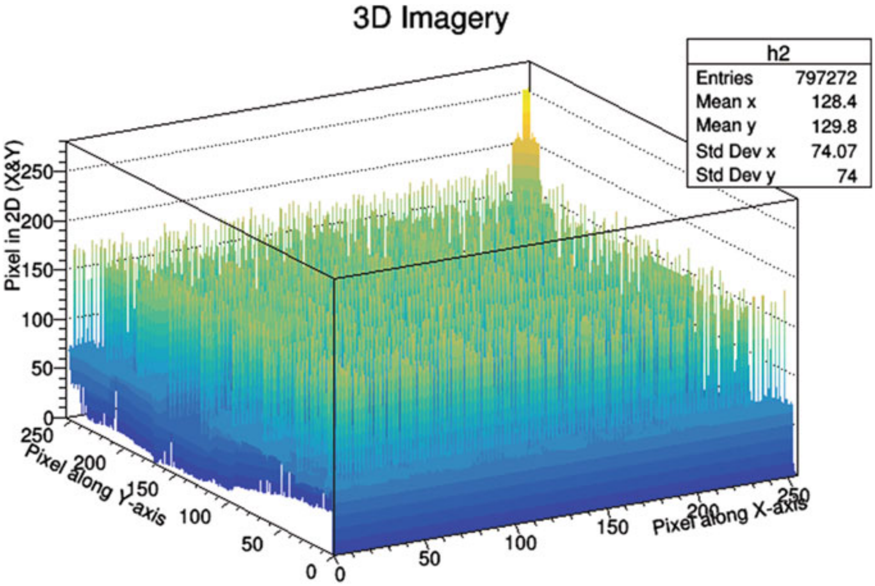

Fig. 4.11 3D setting of satellite image

shows a significant peak around Niger and Chad. This spot was detected in the image contour detection technique in Fig. 4.10.

Figure 4.12 has six main peaks and seven minor peaks. One very interesting concept of image projection is the region of peak (RoP) that depicts the line of highest impact of a given parameter along a specific axis. The main peaks are pixel-40 (Sierra Leone, Guinea, south-west Mali and Mauritania), 80 pixel (Cote d'Ivoire, Mali and Mauritania), pixel-120 (Ghana, Burkina Faso and Mali), pixel-140 (Benin

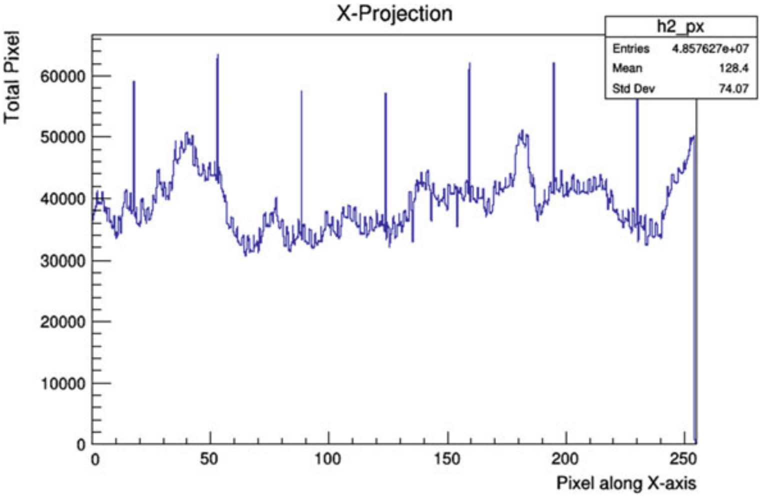

Fig. 4.12 X-projection of satellite image

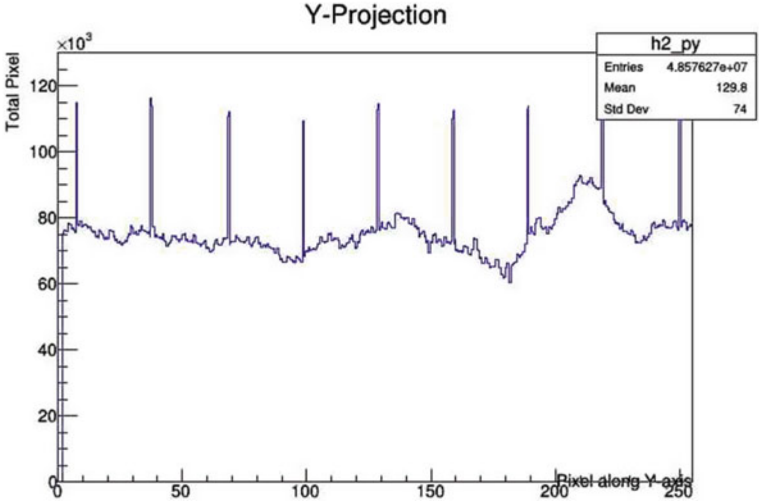

Fig. 4.13 Y-projection of satellite image

and Niger), pixel-180 (Nigeria and Niger) and pixel-250 (northern Cameroun and Chad). The minor peaks are the straight-tiny distinctive lines on Fig. 4.12. They are located on pixel-20 (Guinea, Gambia and Mauritania), pixel-55 (Liberia, Guinea, Mali and Mauritania), pixel-90 (Cote d'Ivoire, Burkina Faso and Mali), pixel-125 (boundary of Ghana and Togo, Burkina Faso and Mali), pixel-160 (Nigeria and Niger), pixel-195 (Nigeria and Niger) and pixel-230 (Cameroun, Nigeria and Chad) (Fig. 4.13).

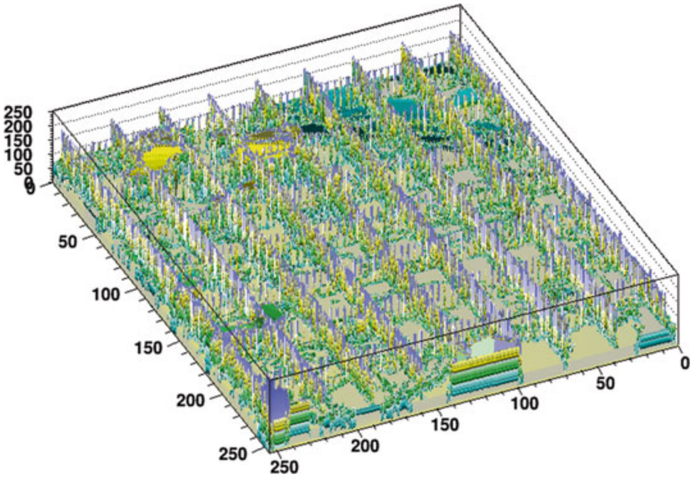

Fig. 4.14 The spectrum analysis of the satellite image

Unlike the X-projection, the Y-projection has one main peak and nine minor peaks. The main peak was at pixel-220 (Mauritania, Mali, Niger and Chad). The minor peaks are pixel-10 (sea), pixel-40 (coastal region of central Liberia, southern Cote d'Ivoire, southern Ghana, southern Togo, southern Benin, southern Nigeria and central Cameroun), pixel-60 (southern Sierra Leone, northern Liberia, central Cote d'Ivoire, central Ghana, central Togo, central Benin, central Nigeria and central Cameroun), pixel-102 (central Guinea, boundary of Mali and Cote d'Ivoire, southern of Burkina Faso, northern Ghana, northern Togo, northern Benin, northern Nigeria, northern Cameroun and central Chad), pixel-130 (Gambia, Guinea Bissau, Mali, Burkina Faso, south-east Niger, northern Nigeria and central Chad), 160 pixel (Senegal, Mali, northern Burkina Faso, Niger and Chad), pixel-190 (northern Senegal, Mauritania, Mali, Niger and Chad), pixel-220 (Mauritania, Mali, Niger and Chad), and pixel-240 (Mauritania, Mali, Niger and Chad).

Figure 4.14 describes how turbulent the mixing ratio of haze or dust or both in the region Fig. 4.8. It means that the particulates from haze and dust are uniform in the tropospheric profile of Fig. 4.8.

Aerosol optical depth is defined as a measure of the extinction of the solar beam by aerosol particulates from dust, haze, bush burning, gas flaring, industrial emission, building emission, automobile emission, domestic emission etc. Green band provides daytime observations related to the land, clouds and aerosols. It is used for air pollution studies and for estimating solar insolation. It is also used to estimate peak vegetation, which is salient for assessing plant vigor. The estimation of peak vegetation is possible when the green band is used to distinguish soil from vegetation. MIL3DAE (v 1, 2) is a product of the Multi-angle Imaging SpectroRadiometer (MISR) level 2 for land surface. It is prominent in determining the component global

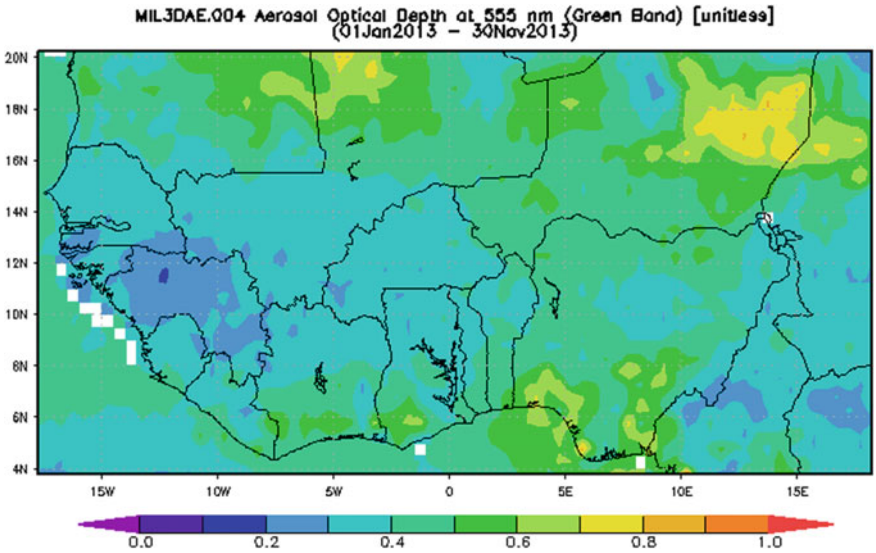

Fig. 4.15 Satellite image AOD at 555 nm, Jan. to Nov., 2013

aerosol product covering per day. Hence, the information on Fig. 4.15 illustrates AOD during the day over the study area.

In Fig. 4.15, the influence of Sahara dust during the day over Mauritania Mali, Niger and Chad. Niger has the highest concentration of dust during the day. Also, it can be inferred from Fig. 4.15 that the concentration of anthropogenic pollution source is from the southern Nigeria, coastal part of Ghana and Cote d'Ivoire. Also, the region of very low AOD can be seen in large area of Guinea and minute parts of Nigeria, Cameroun, Senegal, Mali, Burkina Faso and Cote d'Ivoire.

Figure 4.16 show a clearer color representation of the satellite image. It is very easy to understand the sources of day pollution and the dispersion path that can be described by the red circle. The purple line describes the second concentric aerosol flow path. The speed of the aerosol layers from the source to the secondary destination has been calculated by Emetere (2017). The sources of the daylight pollution had been discussed in Fig. 4.15. However, the dispersion path of aerosol during the day shows that it cuts-through Nigeria. Togo, Benin, Ghana, Cote d'Ivoire, Liberia into the coastal path of Sierra Leone, Guinea, Guinea Bissau, Gambia, Senegal, and Mauritania. The path continues inland Mauritania, Mali and Niger.

Figure 4.17 show the different contour within each big circles. It is observed that the circles describe the aerosol flow path that was discussed in Fig. 4.16. Figure 4.18 show that some geographical areas does not have background aerosol concentration (BAC). The BAC for the affected location is very high. Hence, like the AEOD, the BAC is high at the lower atmosphere of Fig. 4.15.

The X-projection has ten peaks at pixel-40 (Sierra Leone, Guinea, Mali and Mauritania), pixel-80 (Cote d'Ivoire and Mali), pixel-95 (Cote d'Ivoire, Burkina Faso and

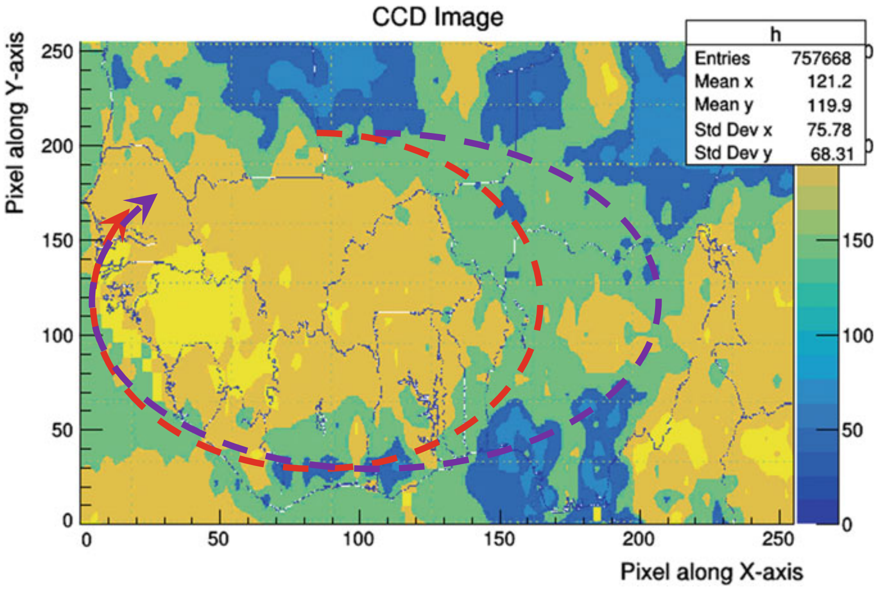

Fig. 4.16 x and y pixel redefinition of the satellite image

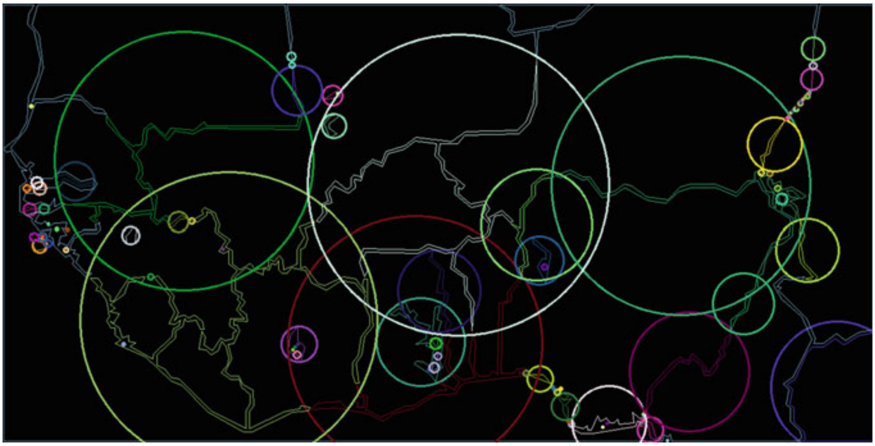

Fig. 4.17 Contour detection of satellite image

Mali), pixel-105 (Cote d'Ivoire, Burkina Faso and Mali), pixel-125 (Ghana, Burkina Faso and Mali), Pixel-135 (Togo, Burkina Faso and Mali), pixel-175 (Nigeria and Niger), pixel-185 (Nigeria and Niger), pixel-200 (Cameroun, Nigeria and Niger) and pixel-220 (Cameroun, Nigeria and Niger). The highest peak can be found at peak-40. Mali, Niger and Burkina Faso were the most affected cities based on the frequency of the location mentioned under the peak. It was observed that all the nations along the aerosol flow path (Fig. 4.16) were mentioned on all the peak location. Hence, it

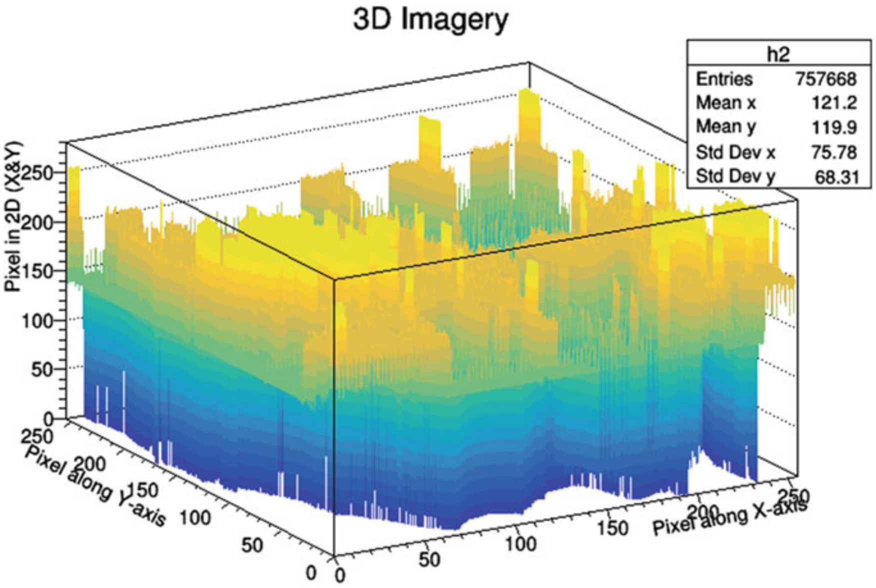

Fig. 4.18 3D setting of satellite image

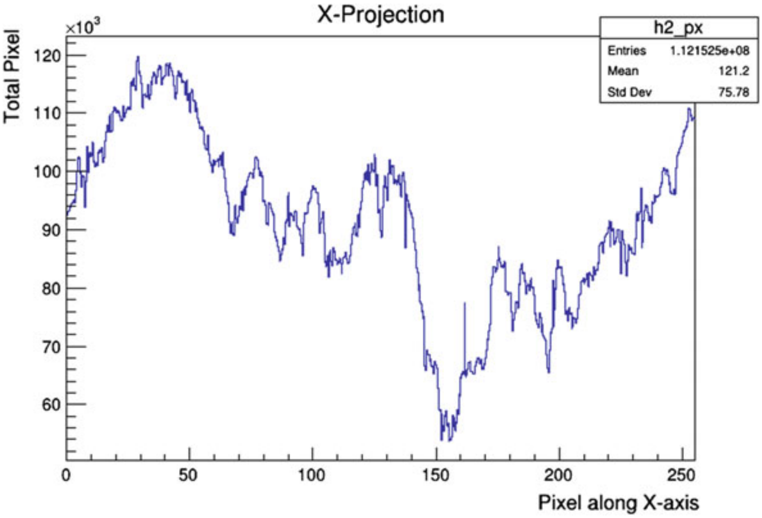

Fig. 4.19 X-projection of satellite image

is trivial to infer that the peak location may also describe the aerosols flow path. The sinusoidal nature of the image feature in Fig. 4.19 may be due to the very unique aerosol flow path for AOD 550 nm.

Figure 4.20 describes the Y-projection. It has three major peaks and two minor peaks. The major peaks are pixel-5 (sea), pixel-45 (Liberia, southern Cote d'Ivoire,

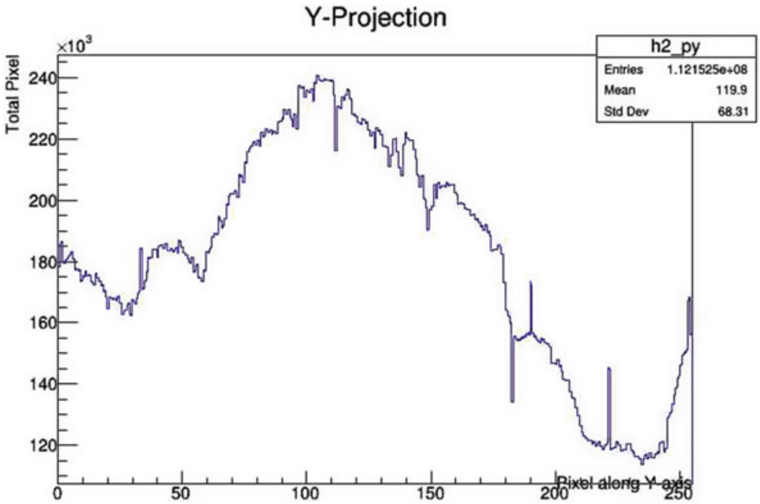

Fig. 4.20 Y-projection of satellite image

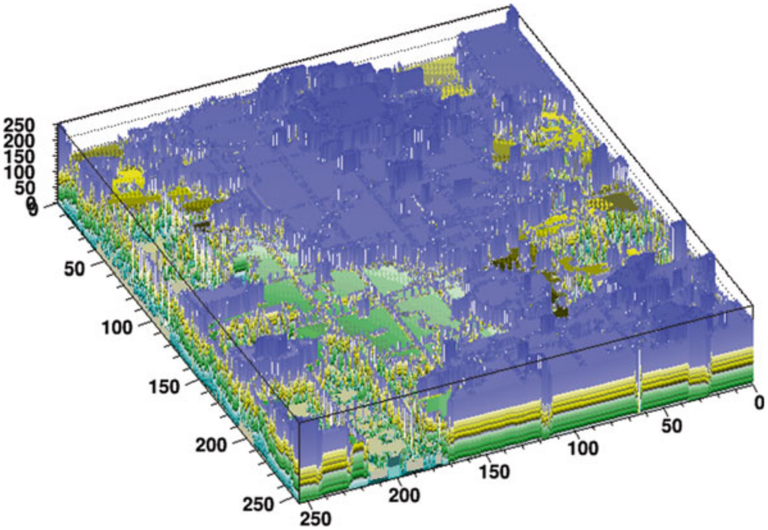

Fig. 4.21 The spectrum analysis of the satellite image

southern Ghana, southern Togo, southern Benin, southern Nigeria and central Cameroun) and pixel-110 (Guinea, southern Mali, southern Burkina Faso, northern Ghana, northern Togo, northern Benin, northern Nigeria, northern Cameroun and southern Chad). The minor peaks are pixel-40 (Senegal, southern Mali, northern Burkina Faso, northern Nigeria and Chad) and pixel-220 (Mauritania, Mali, Niger and Chad). From the intersection rule, pixel-220 both on X and Y projections show that the Niger is the most affected (Fig. 4.21).

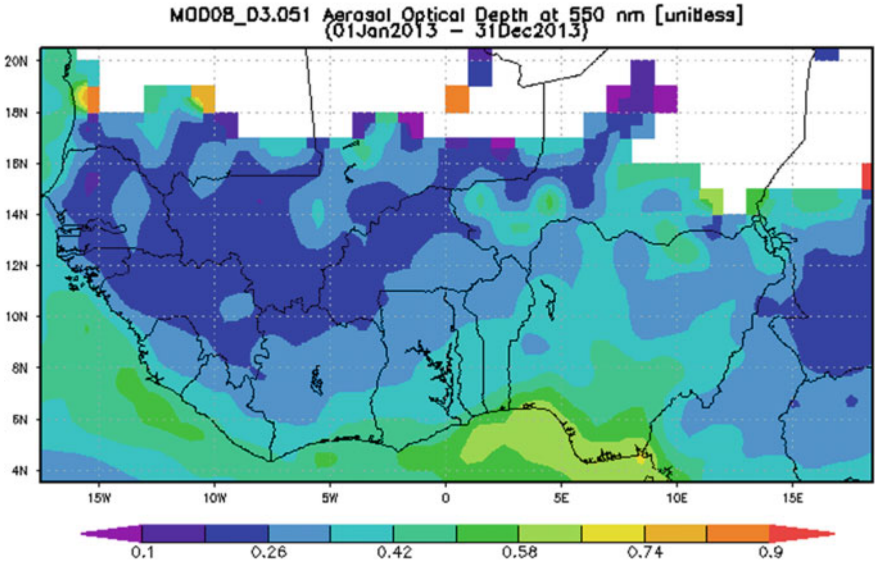

Fig. 4.22 Satellite image AOD at 550 nm, Jan. to Dec., 2013

Figure 4.12 show that the vertical profile of AOD during the day is fairly stable in some parts. This could be explained by the kind of wind dynamics that has been reported over West Africa. The turbulence in the vertical profile can be seen in Niger, northern parts of Nigeria, Chad, northern Cameroun, Mauritania, Senegal and Liberia.

AOD 550 was obtained from the Moderate Resolution Imaging Spectroradiometer (MODIS) Level 2 (MOD08_D3.051). In Fig. 4.22, it was observed that the data in the upper part was distorted. Hence, the information on the Mauritania, Mali, Niger and Chad was not given. The MODIS satellite image show large aerosols concentration at the coastal parts of Nigeria and over the sea. Figure 4.23 show vividly the high AOD concentration observed at the sites of Sierra Leone and Liberia. Secondly, the aerosol flow parts can be seen (red circle) which corroborates the observations in Fig. 4.16. The second aerosols flow path can be seen (purple line). Like Fig. 4.16, Guinea, northern Sierra Leone, northern Liberia, northern Cote d'Ivoire, northern Ghana, Burkina Faso and southern Mali has low AOD during the day (Fig. 4.23). Despite the distortion in Fig. 4.22, it was observed that some parts in the re-processed image (Fig. 4.23) still show high concentration of aerosols in Mauritania, Mali and Niger.

Figure 4.24 shows three large circles over Nigeria, Benin, Togo, Ghana and eastern Cote d'Ivoire. This means that aside the information that is discussed in Fig. 4.23, there are other hotspots that may not be adequately illustrated. This observation is very important in planning ground measurement over a geographical area that the researcher do not have pre-information on Emetere (2016b). Figures 4.18 and 4.25

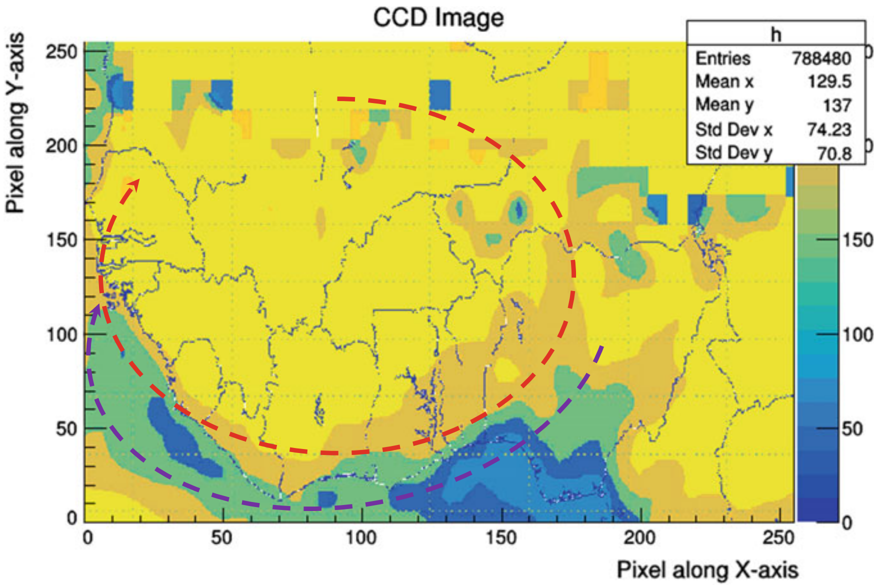

Fig. 4.23 x and y Pixel redefinition of the satellite image

Fig. 4.24 Contour detection of satellite image

shows that the sea does not have background aerosol concentration (BAC). The BAC for the inland is equally high as shown in Fig. 4.25. Contrary to Fig. 4.18, the higher troposphere is characterized by low AOD.

Figure 4.26 has nine peaks i.e. pixel-22 (Guinea Bissau, Gambia, Senegal and Mauritania), pixel-40 (Sierra Leone, Guinea, southern Mali and Mauritania), pixel-65 (Liberia, Guinea, Mali and Mauritania), pixel-80 (Cote d'Ivoire and Mali), pixel-

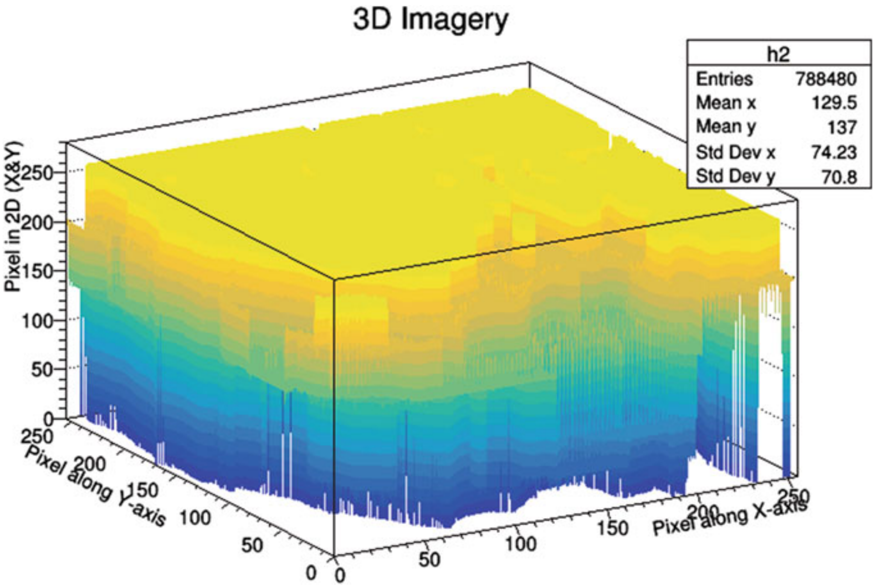

Fig. 4.25 3D setting of satellite image

110 (Ghana, Burkina Faso and Mali), pixel-120 (Ghana, Burkina Faso and Mali), pixel-145 (Nigeria, northern Benin, south Niger and Mali), pixel-165 (Nigeria and Niger) and pixel-215 (Cameroun, Nigeria and Niger). From the frequency of location observed on each peak, it could be concluded that the highest concentration can be found in Mali, Niger and Nigeria.

In Fig. 4.27, two peaks were observed. The peaks were pixel-120 (Guinea Bissau, Guinea, southern Mali, Burkina Faso, northern Benin, Nigeria, northern Cameroun and Chad), pixel-200 (Mauritania, Mali, Niger and Chad). The intersection rule shows that the location with the highest AOD at 550 nm were Burkina Faso and Mali. The inclusion of distortion in the satellite image may compromise the image re-processing technique. For example, the inclusion of Burkina Faso as region of highest AOD is false because of the preceding results shown in Figs. 4.22 and 4.23.

Figure 4.28 shows the turbulence in the vertical profile of Fig. 4.22. It should be noted that the distortion of the AOD image over Mauritania, Mali, Niger and Chad could compromise the turbulence zones in Fig. 4.28. Through the AOD source over Nigeria, vertical turbulence could be seen in the coastline of Nigeria, Benin, Ghana, Cote d’Ivoire and Liberia. It was also observed that the turbulence extended inland towards Guinea. This further confirms that aerosol transport may follow the Gaussian path as expressed in the Gaussian plume model (Walcek 2004; Tirabassi et al. 2010).

The aerosol absorption optical depth (AAOD) at 500 nm was obtained from OMI OMAERUVd v003. OMI OMAERUVd v003 are popularly known as the OMI-Aura level-3. It is an enhanced algorithm developed by NASA Goddard Earth Sciences Data and Information Services Center (GES DISC). AAOD are used to calculate the

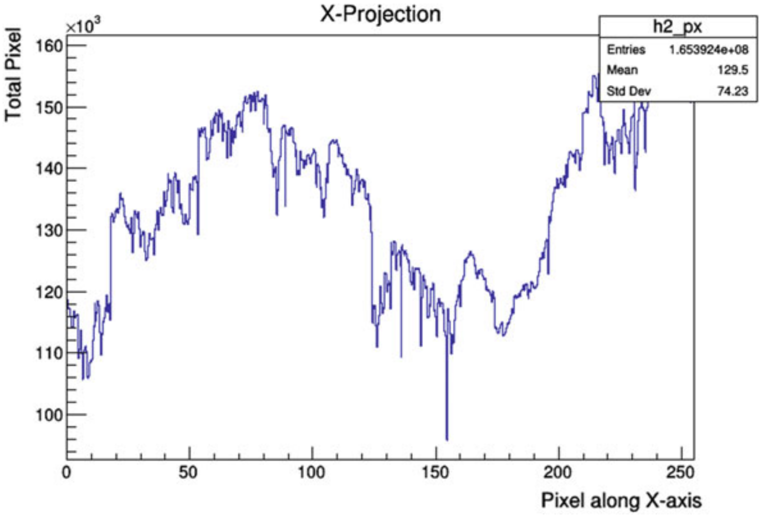

Fig. 4.26 X-projection of satellite image

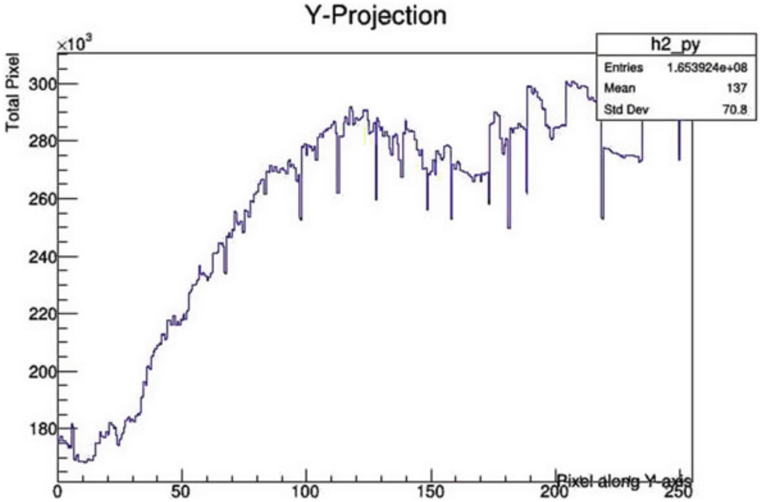

Fig. 4.27 Y-projection of satellite image

radiative forcing of black carbon (BC) aerosols (Bond et al. 2013; Koike et al. 2014). Bond and Bergstrom (2006) defined absorbing aerosol as soot. In this section, the type of AOD considered are the soot or black carbon obtained from bush burning, gas flaring, industrial burning etc. Figure 4.29 shows that there is a large concentration of black carbon in the southern parts of Nigeria. Some parts of Benin and Cote d'Ivoire were observed to have high concentration of black carbon. It was observed that the sea close to Cape Verde and Chad have high concentration of black carbon. Also,

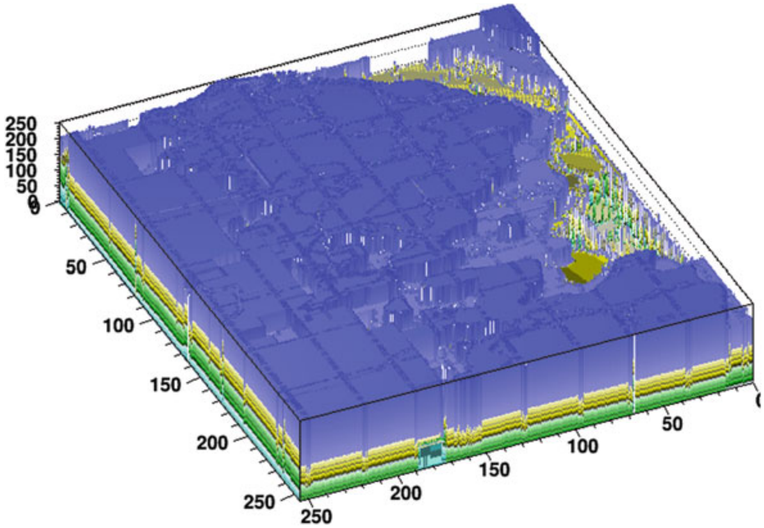

Fig. 4.28 The spectrum analysis of the satellite image

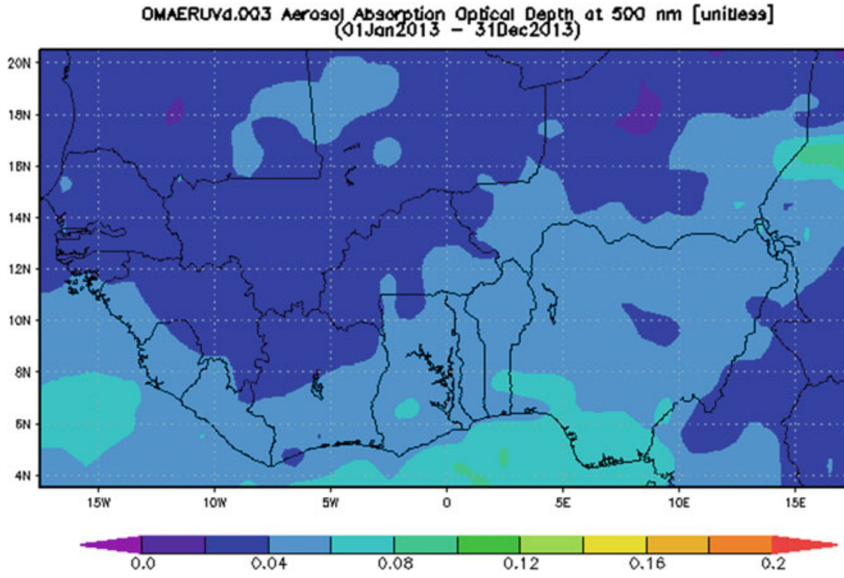

Fig. 4.29 Satellite image AAOD at 500 nm, Jan. to Dec., 2013

about 57% of the study area have low concentration of black carbon. The re-processed image is shown in Fig. 4.30.

In Fig. 4.30, it was observed that the processed image merged two colours located at concentration of 0.04. This makes it very clear that about 92% of the study area

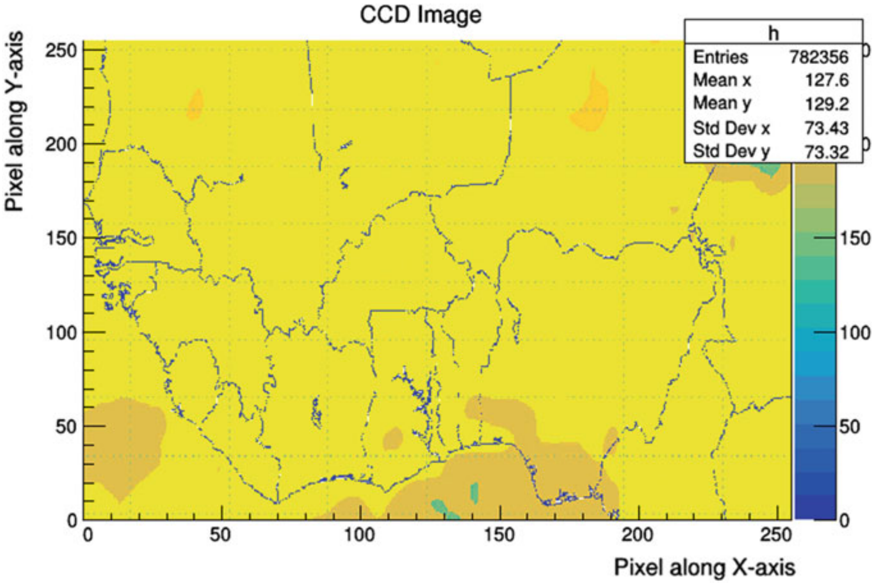

Fig. 4.30 x and y pixel redefinition of the satellite image

have low concentration of black carbon. Hence, the black carbon contributes the lowest fraction of aerosols over West Africa. Figure 4.31 show very striking features that may not be described in the satellite image. First, the circle located at the north-central of Nigeria. A visible contour can be observed inside the circle. Secondly, the red circle over Chad, Nigeria and Niger. Thirdly, two circles over Mali and Mauritania that show significant contours. Other circles were not recon with because it is either over a group of countries or tiny spots along boundaries between two or more countries.

Figure 4.32 shows that the BAC of the lower atmosphere in the region is reasonably high. It also shows that the black carbon concentration in the upper troposphere is very low. Also, it shows that the coastline towards the sea had no BAC. Like previous results, the imagery over the sea on the satellite image is largely due to the influx of aerosol from a primary source(s) close to the coastline.

Figure 4.33 show no significant peak. This means that the black soot concentration is cumulatively low and uniform along the x-axis of the satellite image. However, the Y-projection shows a large variation (Fig. 4.33) with eleven peaks. The peaks are pixel-10 (sea), pixel-20 (coastline), pixel-40 (southern Liberia, southern Cote d'Ivoire, southern Ghana, southern Togo, southern Benin, southern Nigeria and northern Cameroun), pixel-55 (southern Sierra Leone, northern Liberia, southern Guinea, central Cote d'Ivoire, central Ghana, central Togo, central Benin, central Nigeria, northern Cameroun and southern Chad), pixel-70 (Sierra Leone, Guinea, Cote d'Ivoire, Ghana, Togo, Benin, Nigeria, Cameroun and Chad), pixel-85 (Sierra Leone, Guinea, Cote d'Ivoire, Ghana, Togo, Benin, Nigeria, Cameroun and Chad),

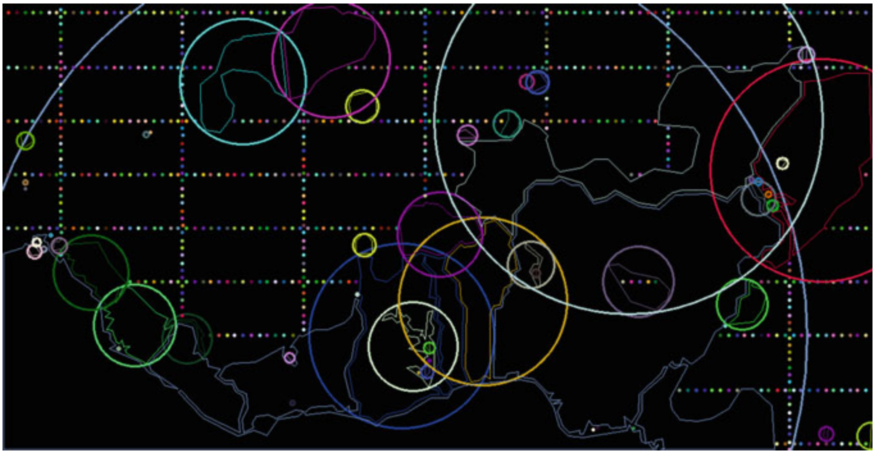

Fig. 4.31 Contour detection of satellite image

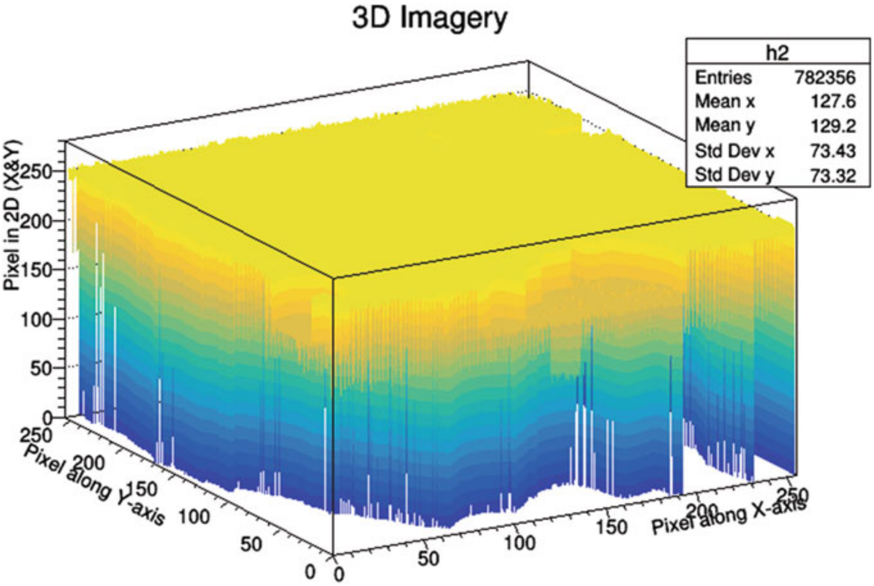

Fig. 4.32 3D setting of satellite image

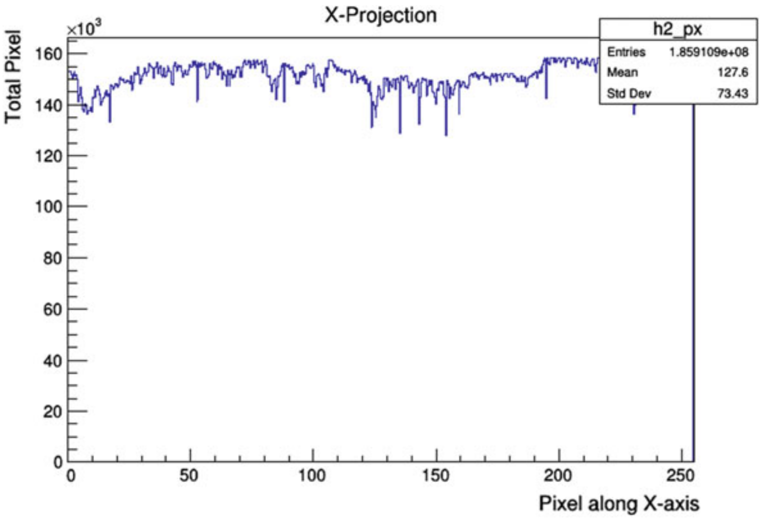

Fig. 4.33 X-projection of satellite image

pixel-120 (Guinea Bissau, Guinea, Mali, Burkina Faso, northern Benin, northern Nigeria, northern Cameroun and Chad), pixel-140 (Senegal, Mali, Burkina Faso, Niger and Chad), pixel-170 (Senegal, Mali, Burkina Faso, Niger and Chad), pixel-185 (Senegal, Mauritania, Mali, Niger and Chad) and pixel-220 (Mauritania, Mali, Niger and Chad). Neither the frequency rule nor the intersection rule can be applied in this sense since one of the 2D axis (x-axis) shows that the distribution of the black soot is almost uniform. The vertical profile can also be adjudged as uniform (Fig. 4.35). It can be seen that the vertical-profile of the black soot over the study fluctuates slightly.

The AAOD at 388 nm was considered in Fig. 4.36. Recall that the AAOD at 500 nm was earlier discussed in Figs. 4.29, 4.30, 4.31, 4.32, 4.33, 4.34 and 4.35. 388 nm means that the satellite image is been viewed from a closer perspective. Hence, this Figure is insightful to validate the vertical profile analysis of previous figures. First, the satellite image (Fig. 4.36) shows that below the vertical profile of Fig. 4.29, high source of black carbon can be seen between the boundaries of Mauritania and Mali. Secondly, more area under the image shows higher black carbon concentration. This shows that the area has significant presence of black carbon in its background. The transport or dispersion of the black carbon from its source to the upper troposphere or lower stratosphere depends on the wind dynamics, concentration level of black carbon, life-time and existing aerosol retention in the upper troposphere.

Figure 4.37 shows a clearer picture of aerosol flow path that was discussed earlier. The new color representation helps to identify location of unique features. For example, it can be clearly seen that there are six spots (first spot at the offshore of Ghana, Togo and Benin, second spot at the offshore of Nigeria, third spot at the boundary of Mauritania and Mali, fourth spot in Mali, fifth spot in Niger, and sixth spot at the

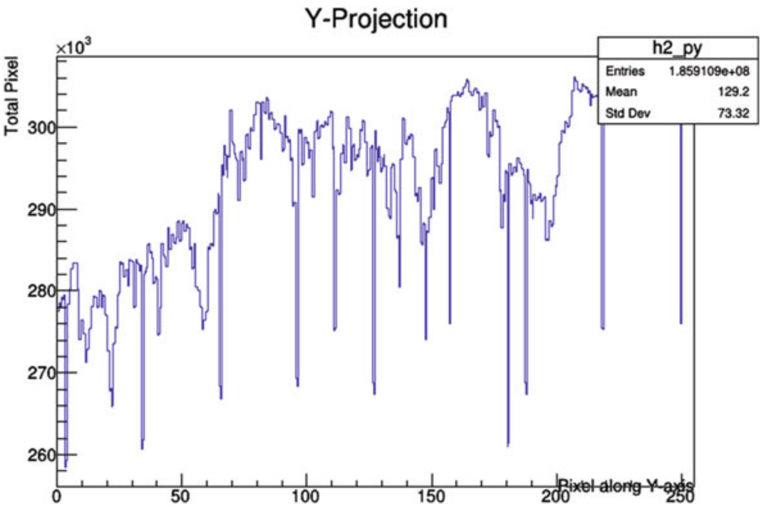

Fig. 4.34 Y-projection of satellite image

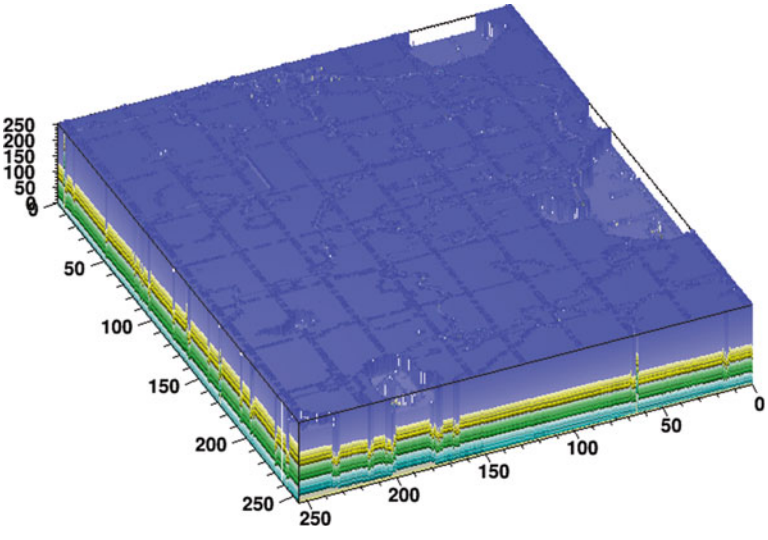

Fig. 4.35 The spectrum analysis of the satellite image

boundaries of Niger and Chad) that may show the source of black carbon. This image shows more interesting black carbon deposition in the coastline of West Africa.

Figure 4.38 shows the five drawing defect as shown in Fig. 4.36. The sensitivity of the contour detection is high and can be used to understand the bigger circles within the study area. For example, the green (biggest) circle shows a unique trend of black carbon catchment in Fig. 4.36. Comparing Figs. 4.38 and 4.31, it can be observed

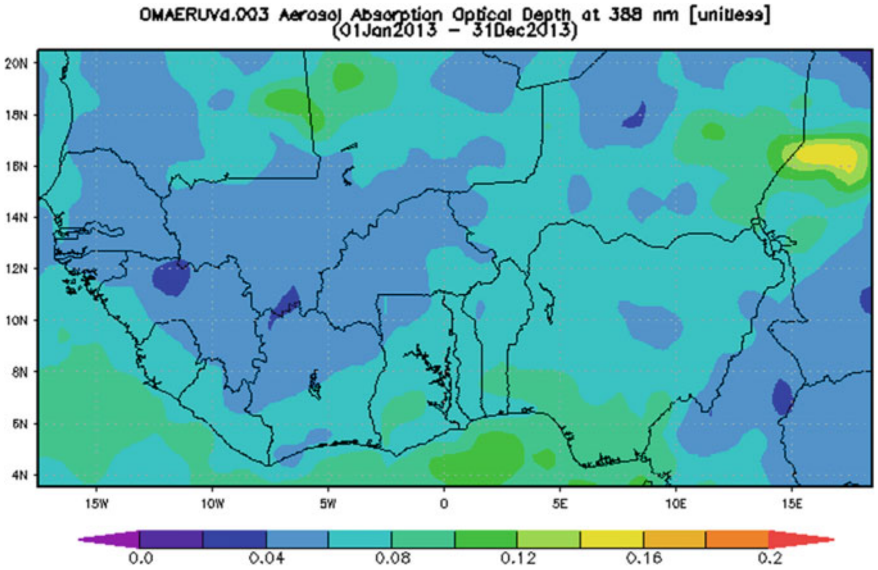

Fig. 4.36 Satellite image AAOD at 388 nm, Jan. to Dec., 2013

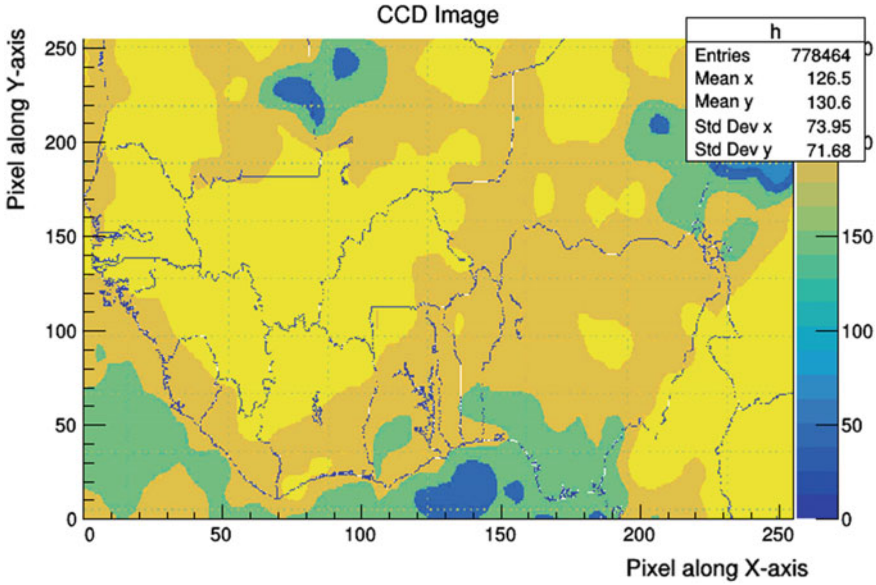

h	
Entries	778464
Mean x	126.5
Mean y	130.6
Std Dev x	73.95
Std Dev y	71.68

Fig. 4.37 x and y pixel redefinition of the satellite image

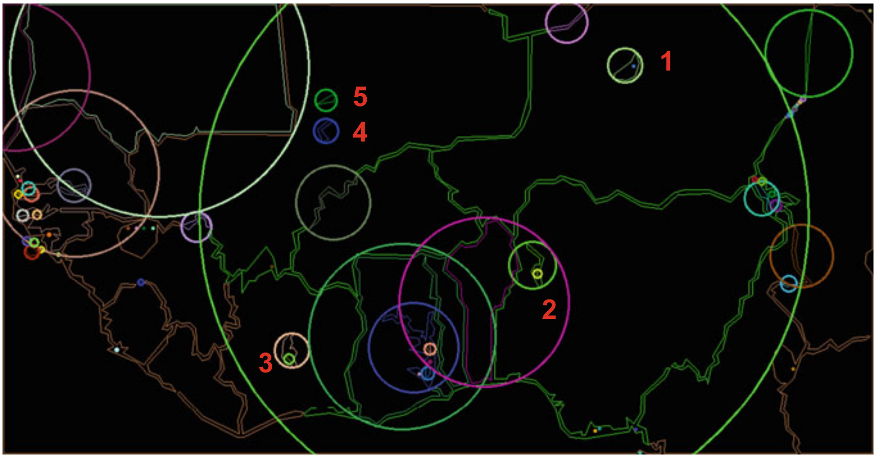

Fig. 4.38 Contour detection of satellite image

that the contour detection pattern differs. This means that even at different vertical profile, layers of aerosols (which are invisible to the naked eye) can be identified.

The BAC in Figs. 4.32 and 4.39 are almost similar. This affirms that the 3D image could give the approximate BAC of an image. The scanty top of Fig. 4.39 describes that there is more concentration of black carbon at the mid troposphere. The X-projection of Fig. 4.40 show more activity compared to Fig. 4.33. It has a sinusoidal feature that depicts positional variation along the x-axis.

Figure 4.40 has ten peaks i.e. pixel-35 (Sierra Leone, Guinea, Senegal and Mauritania), pixel-60 (Liberia, Guinea, southern Mali and Mauritania), pixel 70 (Cote d'Ivoire, Mauritania and Mali), pixel-90 (Cote d'Ivoire, Burkina Faso and Mali), pixel-100 (Cote d'Ivoire, Burkina Faso and Mali), pixel-110 (Ghana, Burkina Faso and Mali), pixel-130 (Togo, Burkina Faso, southern Niger and Mali), pixel-170 (Nigeria and Niger), pixel-185 (Nigeria and Niger), pixel-200 (Cameroun, Nigeria and Niger). From the frequency rule, Mali had the highest concentration of black carbon on the x-projection. Figure 4.41 show the Y-projection of the satellite image.

There are five peaks in Fig. 4.41. They are pixel-20 (coastline of Liberia, coastline of Cote d'Ivoire, coastline of Nigeria and Cameroun), pixel-90 (Sierra Leone, Guinea, Cote d'Ivoire, Ghana, Togo, Benin, Nigeria, and Cameroun), pixel-100 (Guinea, Cote d'Ivoire, Ghana, Togo, Benin, Nigeria, northern Cameroun and Chad), pixel-140 (Senegal, Mali, Burkina Faso, southern Niger, Nigeria and Chad) and pixel 165 (Senegal, Mali, Burkina Faso, Niger and Chad). By the frequency rule, Nigeria has the highest concentration along the y-axis. By the intersection rule, Pixel-90 on both (x and y) projections (Cote d'Ivoire) and pixel-100 on both projections (Cote d'Ivoire). The spectrum analysis of the satellite images (Fig. 4.42) show the high perturbation in the vertical profile. More so, the aerosol flow path had higher perturbation in the vertical profile.

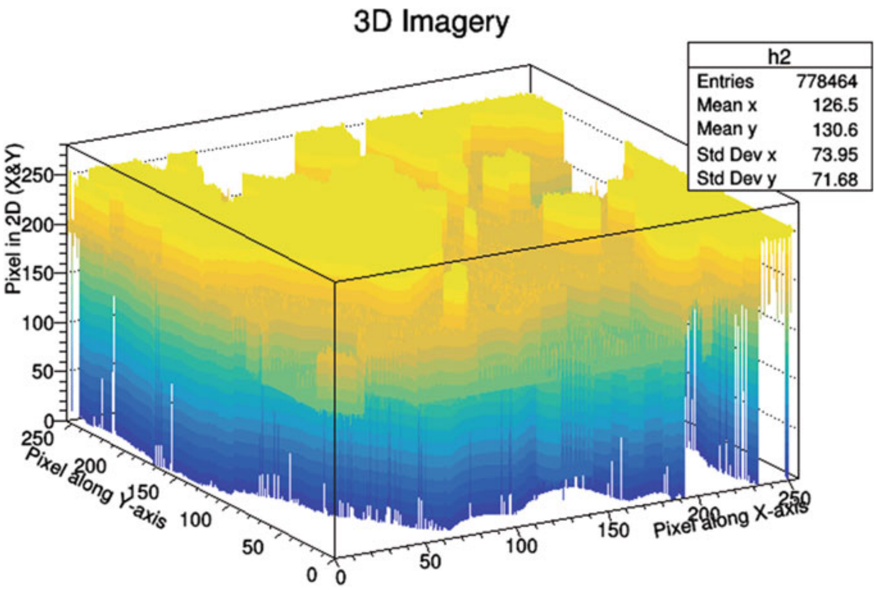

Fig. 4.39 3D setting of satellite image

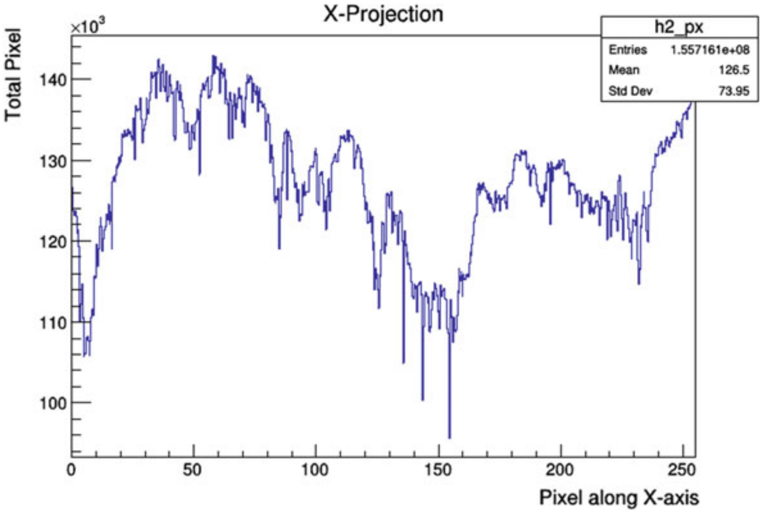

Fig. 4.40 X-projection of satellite image

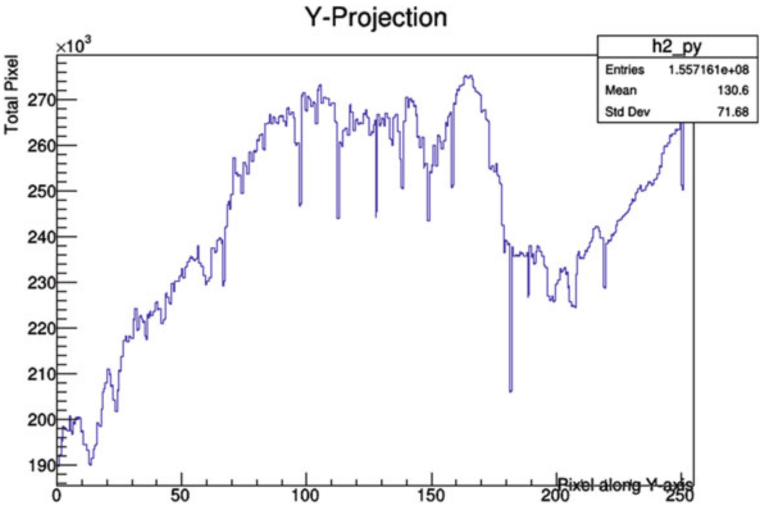

Fig. 4.41 Y-projection of satellite image

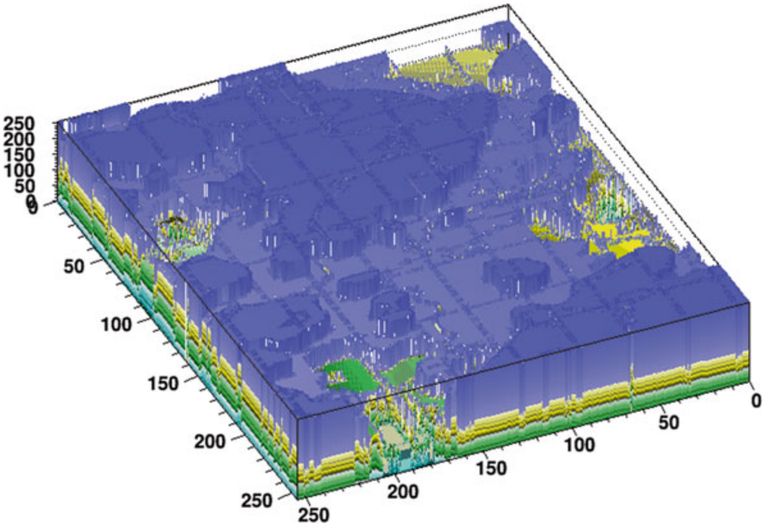

Fig. 4.42 The spectrum analysis of the satellite image

AEOD at 388 nm had been discussed in Fig. 4.8. Figure 4.43 show the AEOD at 500 nm. Generally, AEOD describes the level of impact on direct and indirect aerosol forcing (Lacis and Mishchenko 1995). A type class of aerosol that affects AEOD is the tropospheric sulfate (Tegen et al. 1997). Figure 4.43 show that the region of highest concentration was Chad, Niger, Mali and Mauritania. Coincidentally, the same region had high black carbon. Hence the anthropogenic pollution of the location will be very interesting to study. Figure 4.44 clearly show the aerosol flow path of the

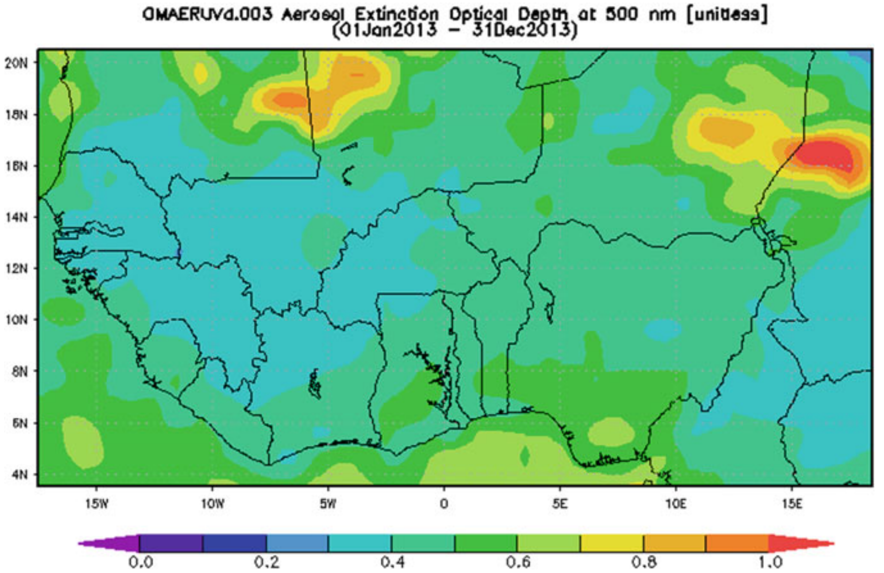

Fig. 4.43 Satellite image AEOD at 500 nm, Jan. to Dec., 2013

satellite image. Like the AAOD—Fig. 4.37, the sea at the coastline of West Africa had high AEOD. Hence Fig. 4.44 shows seven hotspots i.e. south-south of Nigeria (hotspot 1), offshore of Nigeria, Benin, Togo and Ghana (hotspot 2), offshore of Cote d'Ivoire (Hotspot 3), offshore of Sierra Leone and Liberia (Hotspot 4), boundary of Niger and Chad (hotspot 5), boundary of Niger and Mali (hotspot 6) and boundary of Mali and Mauritania (hotspot 7). The contour detection in Fig. 4.45 show same big circle (like Fig. 4.38) that describe the aerosol flow path.

Figure 4.46 shows a high BAC inland and no or little BAC offshore. From the surface of the 3D image, it can be inferred that the extinction aerosol is generally high. The X-projection has six peaks i.e. pixel-35 (Sierra Leone, Guinea, Senegal and Mauritania), pixel-75 (Cote d'Ivoire, Mali and Mauritania), pixel-110 (Ghana, Burkina Faso and Mali), pixel-130 (Togo, Burkina Faso, southern Nigeria and Mali), pixel-180 (Nigeria and Niger) and pixel-205 (Cameroun, Nigeria and Niger). By the frequency rule, Niger has the highest AEOD. Figure 4.48 show that Y-projection has a Gaussian distribution with its peak at pixel-120 (Guinea Bissau, Guinea, Mali, Burkina Faso, northern Benin, Nigeria, northern Cameroun and Chad) (Fig. 4.47).

However, there were some minor peaks along the Gaussian distribution located at pixel-35 (Liberia, Cote d'Ivoire, Togo, Benin, Nigeria and Cameroun), pixel-185 (Senegal, Mauritania, Niger, Mali and Chad) and pixel-220 (Mauritania, Mali, Niger and Chad). The frequency and the intersection rule cannot hold because of the Gaussian distribution. Figure 4.49 show the degree of vertical profile turbulence. Therefore, AEOD at 500 nm show how much the area is influenced by sulfate aerosols.

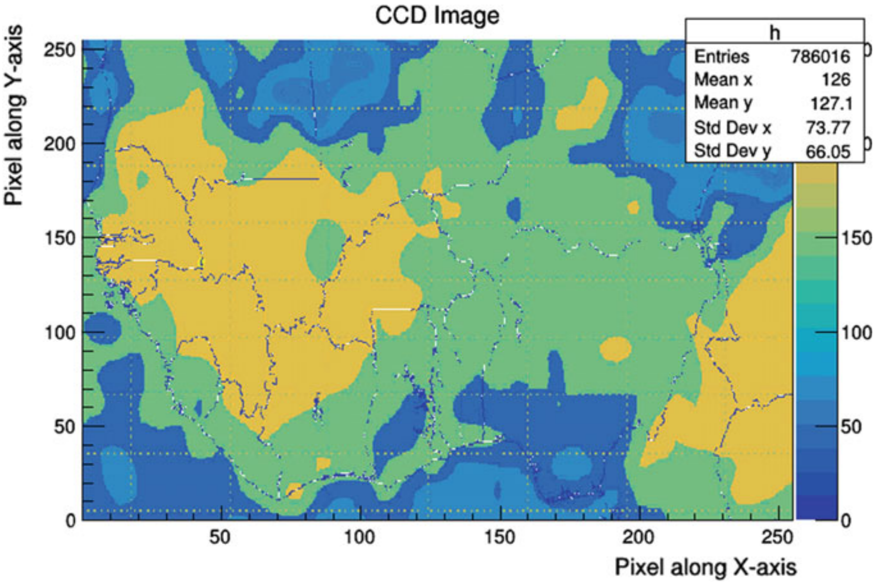

Fig. 4.44 x and y pixel redefinition of the satellite image

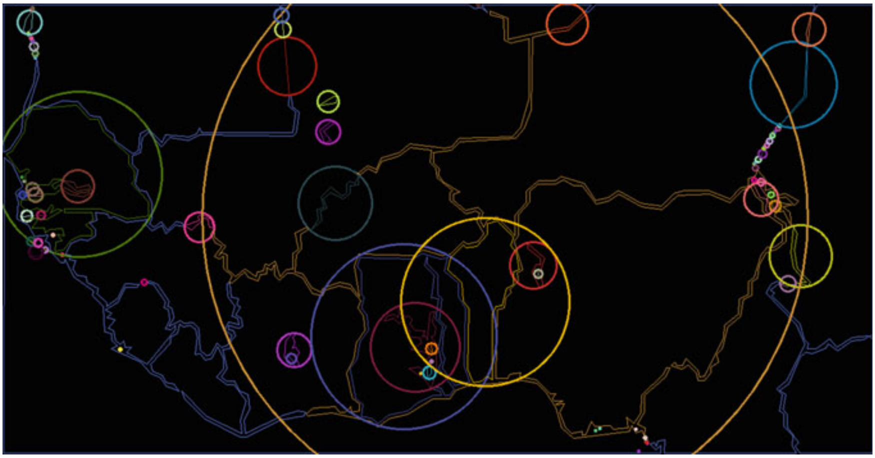

Fig. 4.45 Contour detection of satellite image

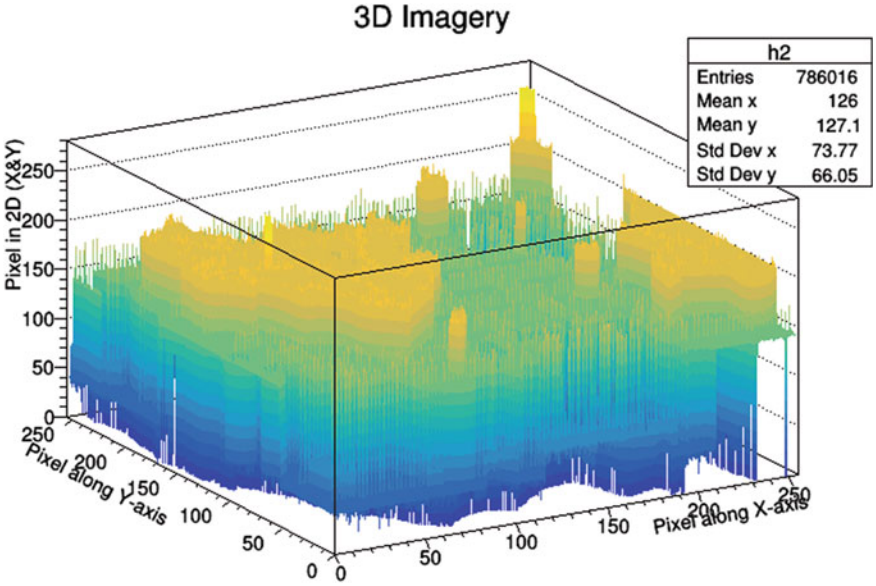

Fig. 4.46 3D setting of satellite image

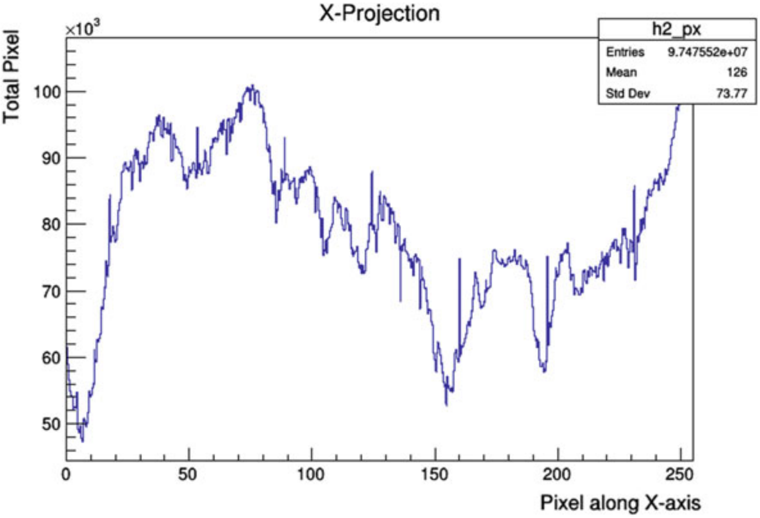

Fig. 4.47 X-projection of satellite image

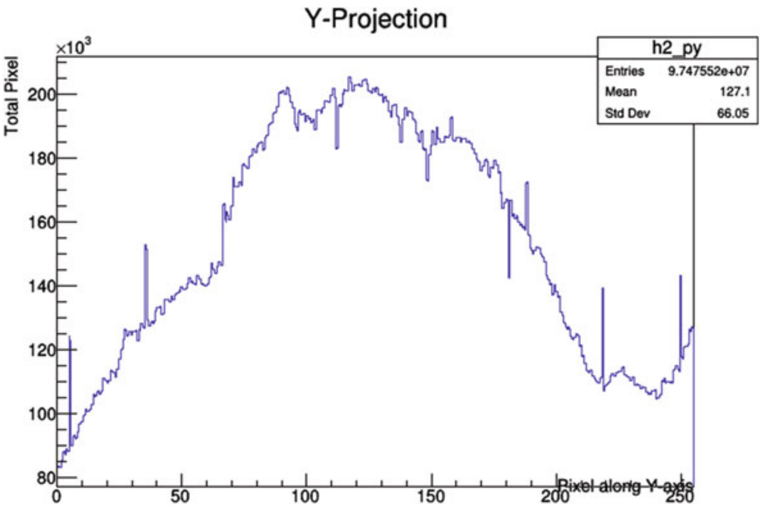

Fig. 4.48 Y-projection of satellite image

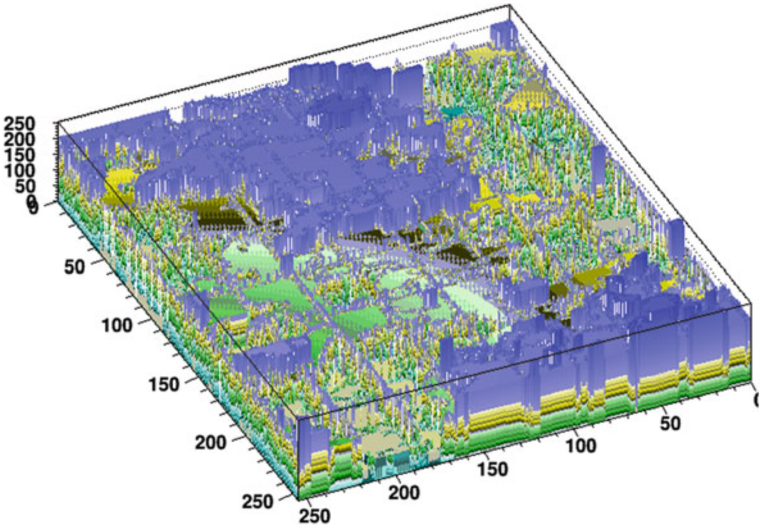

Fig. 4.49 The spectrum analysis of the satellite image

4.2 Implication of Computational Outcomes

In the last section, it can be inferred that the image re-processing technique draws-out more information about the satellite image in that: it re-maps the original satellite image (in distinctive colours) for better understanding of its hidden features; it shows aerosol concentration hotspots (via contour detection) that may not be seen by the ordinary eye; it provides the background aerosol concentration (BAC) of an area and spatial distribution of aerosols at the upper troposphere/lower stratosphere; it shows the image projections in the x and y axis; and it shows the degree of vertical profile turbulence.

It was also discussed in the last section that the most active regions of a satellite image can be determined by the frequency and intersection rule of the locations listed under the peaks of the X and Y projection. The peaks in the X and Y projection were classified as major or minor peaks. For example, in Figs. 4.12 and 4.13, the worst hit places by dust and haze are Mauritania, Mali, Niger and Chad; followed by Burkina Faso, Cote d'Ivoire, Ghana, Togo, Benin, Nigeria and Cameroun. By the intersection rule (i.e. major or minor peaks at ≤ 5), the close peak intersection in both the X and Y projections are pixel-55 (X-projection) and pixel-60 (Y-projection), pixel-125 (X-projection) and pixel-130 (Y-projection), pixel-160 (X-projection) and pixel-160 (Y-projection), pixel-195 (X-projection) and pixel-190 (Y-projection). Hence, from the intersection technique, the country that appear in both intersection points are Liberia (first intersection, Burkina Faso and Mali (second intersection), Niger (third intersection), and Niger (fourth intersection). Therefore, it is very logical to conclude that the country that has the highest concentration of dust and haze is Niger. However, going back on Fig. 4.8, it looks contradictory that the AEOD over Guinea was among the highest but the AOD at 550 nm was the lowest. This contradiction may be explained with respect to the unique transports of aerosol particulates over West Africa (Emetere 2017). Hence, aerosol layers travel from one neighbouring country or community to another.

One of the salient lessons learnt by re-processing satellite images is that aerosol move in a concentric path (red circle in Fig. 4.16) that was christened 'aerosol flow path'. From Figs. 4.16, 4.23, 4.37 and 4.44, the route of the aerosol flow path is from Nigeria, Benin, Togo, Ghana and Cote d'Ivoire—towards the coastal parts of the south-western countries on Fig. 4.15. The route of the aerosol flow path from the north is through Mauritania, Mali, Niger and Chad into northern Nigeria. Two aerosol flow paths were notice over Nigeria. The first aerosol flow path is through the north-west, north central and south west of Nigeria. The second aerosol flow path is through the north-east, north-central, south-east and south-south of Nigeria. This informs our consideration of the data-processing locations in the next chapter.

Figures 4.15 (AOD at 555 nm) and 4.22 (AOD at 550 nm) affirm that the hotspots were located in Ghana and Cote d'Ivoire. Secondly, the AOD (at 555 nm) show that aerosol flow path route along the coastal part of Nigeria and extends inland (Figs. 4.15 and 4.16). Thirdly, AOD 550 nm show a significant extension of the AOD over the sea. In Fig. 4.23, the aerosol flow path can be seen (red circle) which corroborates the observations in Fig. 4.16. The turbulent locations described in Fig. 4.21 do not correspond to the locations mentioned under the aerosol flow path in Fig. 4.16. This suggests that the aerosol flow path takes place at the upper troposphere while the turbulence takes place at the lower atmosphere. Hence, the image re-processing could afford salient information that may not be described on satellite images.

The implication of regions without BAC (over sea) as presented in Figs. 4.18 and 4.25 show that aerosol pollution that is portrayed in the satellite imagery may not be due to movement of ship across the coastal part, but the aerosols transport from pollution sources close to the coastline. The BAC in Fig. 4.32 and 4.39 are almost similar. This affirms that the 3D image could give the approximate BAC of an image.

The main advantage of the re-processed image is its ability to encourage comparative study between two location or same location at different times. In the light of the above, the satellite imagery of the following was processed:

i. Satellite image AAOD at 500 nm, Jan. to Dec., 2007 (Appendix: Figs. A.1–A.7);
ii. Satellite image AEOD at 388 nm, Jan. to Dec., 2007 (Appendix: Figs. A.8–A.14);
iii. Satellite image AOD at 555 nm, Jan. to Dec., 2007 (Appendix: Figs. A.15–A.21);
iv. Satellite image AOD Pixel Counts, Jan. to Dec., 2007 (Appendix: Fig. A.12–A.28);
v. Satellite image AOD, Coarse mode, Jan. to Dec., 2007 (Appendix: Figs. A.29–A.35);
vi. Satellite image AAOD at 388 nm, Jan. to Dec., 2007 (Appendix: Figs. A.36–A.42);
vii. Satellite image ACOD at 550 nm, Jan. to Dec., 2007 (Appendix: Figs. A.43–A.49);
viii. Satellite image ACOD at 550 nm-FM, Jan. to Dec., 2007 (Appendix: Figs. A.50–A.56);
ix. Satellite image AEOD at 500 nm, Jan. to Dec., 2007 (Appendix: Figs. A.57–A.63);
x. Satellite image AOD at 550 nm, Jan. to Dec., 2007 (Appendix: Figs. A.64–A.70).

In the comparative analysis, the satellite image of dust aerosol column optical depth (ACOD) at 550 nm, for the year 2007 (Appendix: Fig. A.43) was used as the standard because dust is the main aerosol content over the research area (Senghor et al. 2017). Figure 4.50 show the X-projection of two types of aerosol parameter [i.e. AAOD at 500 nm for 2007 (indigo) and AAOD at 500 nm for 2013 (blue)] and the standard [i.e. ACOD at 550 nm for 2007 (yellow)]. It can be inferred from Fig. 4.50 that there is about 14.3% increase in AAOD from 2007 to 2013. Second, the AAOD over locations in pixel-205 (north-west Cameroun, north-east Nigeria and Niger) was constant between 2007 and 2013. Third, ACOD cuts across: AAOD-2013 at pixel-18 (Guinea Bissau, Gambia, Senegal and Mauritania); AAOD-2007 at pixel-50 (Liberia, Guinea, Mali and Mauritania); AAOD-2007 at pixel-135 (Benin, Niger and Mali); pixel-145 (Nigeria, Benin, Niger and Mali); pixel-155 (Nigeria and Niger). The intersection points are certainly where the ACOD equals the AAOD. Hence, it could be inferred that AAOD are prominent over the region.

In Appendix-Fig. A.71, the AEOD at 388 nm were almost similar. The ACOD interacted with AEOD (2007 and 2013) between longitude 17°W and 9°W. In Appendix-Fig. A.72, the AOD at 555 nm was nearly similar. The ACOD interacted with AOD (2007 and 2013) throughout the X-projection. AOD pixel count for 2007 and 2013 was similar (Appendix-Fig. A.73). The ACOD interacted with AEOD

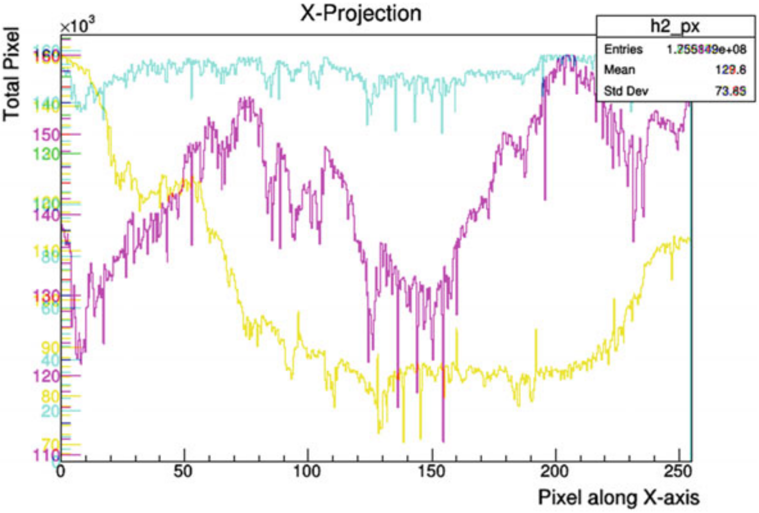

Fig. 4.50 Comparative analysis of AAOD at 500 nm (2007 and 2013) and assumed standard (ACOD 2007) in the X-projection

(2007 and 2013) between longitude 17°W and 14°W. There was less than 2% increase between the AAOD (at 388 nm) in the year 2007 and 2013 (Appendix-Fig. A.74). The ACOD interacted with AAOD at 388 nm (2007 and 2013) between longitude 17°W and 13°W. In Appendix-Fig. A.75, the difference between the AEOD at 500 nm for the year 2007 and 2013 was ≤35%. The ACOD interacted with AEOD (2007 and 2013) throughout the X-projection. Almost same analysis was for Appendix-Fig. A.76 as Appendix-Fig. A.75.

The AAOD increase for each country can be estimated by multiplying the percentage increase/decrease between the two years (2007 and 2013) and AAOD values. For example in pixel-60 for AAOD in 2007, the countries and the corresponding AAOD is Liberia (≈0.08), Guinea (≈0.06), Mali (≈0.05) and Mauritania (≈0.04). The percentage increase at pixel-60 is 6.7%. The multiplication factor is (100 + 6.7)/100. Hence the new value expected in 2013 will be Liberia (≈1.067 * 0.08 = 0.085 along the x-axis), Guinea (≈1.067 * 0.06 = 0.064 along the x-axis), Mali (≈1.067 * 0.05 = 0.053 along the x-axis) and Mauritania (≈1.067 * 0.04 = 0.043 along the x-axis).

The line and color arrangement in Fig. 4.51 is the same as Fig. 4.50. The standard (ACOD 2007) describes a phase-shift parabola while both AAOD (2007 and 2013) exponential-growth parabola. There was no major difference between AAOD for 2007 and 2013. The meeting point of the AAOD and ACOD is at pixel-75 (Cote d'Ivoire, Mali and Mauritania). The Y-projection comparison is shown for AEOD at 388 nm (2007 and 2013), AOD at 555 nm (2007 and 2013), AOD pixel count (2007 and 2013), AAOD (2007 and 2013), AAOD at 388 nm (2007 and 2013), AAOD at 500 nm (2007 and 2013), and AEOD at 500 nm (2007 and 2013). The images are located at Appendix: Figs. A.77–A.82. The AEOD at 388 nm was almost similar with

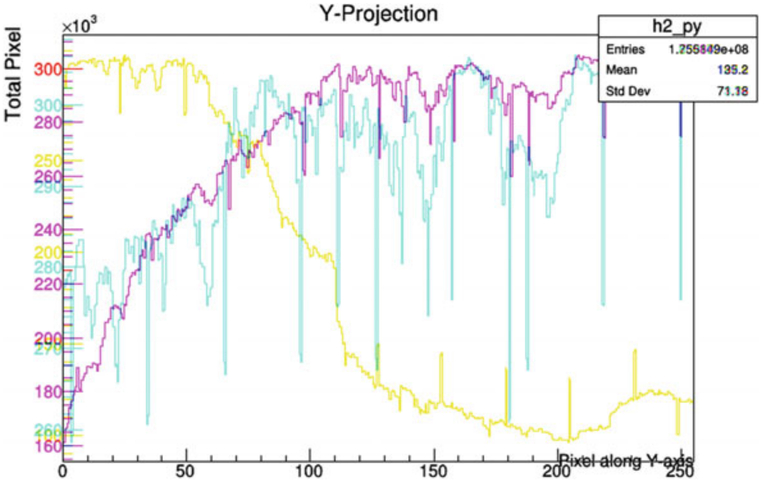

Fig. 4.51 Comparative analysis of AAOD at 500 nm (2007 and 2013) and assumed standard (ACOD 2007) in the Y-projection

AEOD 500 nm. However, there was a large difference between 2007 and 2013 of AEOD at 388 nm (Appendix: Fig. A.77). The percentage increase from 2007 to 2013 was ≤26%. In Appendix: Fig. A.78, both years (2007 and 2013) had Gaussian-like shape. The percentage increase from 2007 to 2013 was ≤33%.

Lastly in this section, the difference between images using the image intensity, mean pixel, standard deviation and full width at half maximum (FWHM) is illustrated below. The satellite image numbers are denoted as follows:

0—AOD pixel count at 388 nm (2013);
1—AEOD at 388 nm (2013);
2—AOD at 555 nm (2013);
3—AOD at 550 nm (2013);
4—AAOD at 500 nm (2013);
5—AAOD at 388 nm (2013);
6—AEOD at 500 nm (2013);
7—AAOD at 500 nm (2007);
8—AEOD at 388 nm (2007);
9—AOD at 555 nm (2007);
10—AOD Pixel Counts (2007);
11—AOD, Coarse mode (2007);
12—AAOD at 388 nm (2007);
13—ACOD at 550 nm (2007);
14—ACOD at 550nm-FM (2007);
15—AEOD at 500nm (2007);
16—AOD at 550nm (2007).

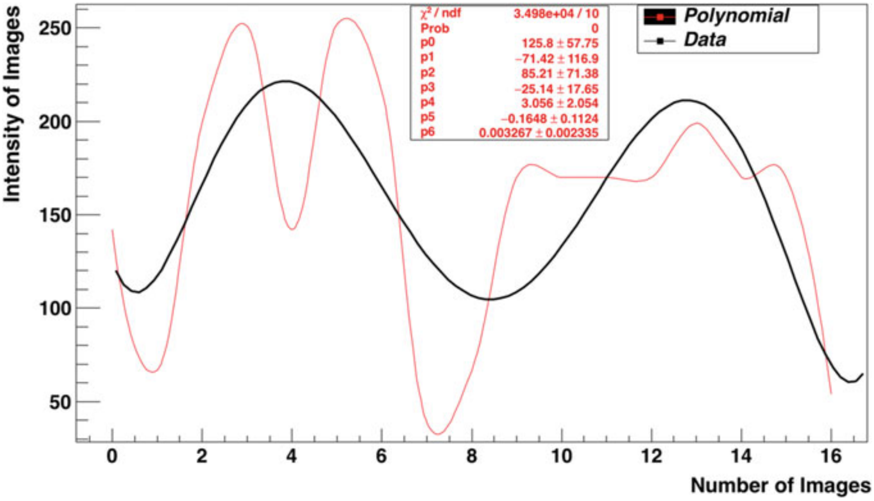

Fig. 4.52 Intensity of satellite images

Figure 4.52 is the intensities of the highlighted images above. It is observed that AOD at 550 nm (2013) and AAOD at 388 nm (2013) had the highest intensities. This means that the above mentioned images have the most significant value of a pixel in an image matrix. The polynomial values are listed to aid optimization when the environmental images are sequential in only one type of dataset.

Figure 4.53 is the mean pixel of the satellite images. AAOD at 388 nm (2007) had the highest image mean-pixel. Hence, the image has the most significant smallest addressable element of the image. AEOD at 500 nm (2013) and AEOD at 500 nm (2007) also had a high mean pixel. In Fig. 4.54, AOD pixel count at 388 nm (2013) had the highest standard deviation among images. Also in Fig. 4.55, AOD pixel count at 388 nm (2013) had the highest standard deviation among images.

4.3 Planning the Code Design

In this section, the discussion shall be on how to design the code used for running the above simulations. Planning the design of a code is paramount to the desired goal of the research (i.e. using computational process). Codes may be written in macro or compiled program. A program is an executable script that assists the computer system to execute specific instructions. The executable instructions are compiled using computer language such as C, C++ etc. The executable instructions are arranged in a modular manner, with good separation of subsections. Macro is usually something more simple and ad hoc. The common usage of macros is in software applications for mapping user input to different set of user output. Program makes use of larger tools

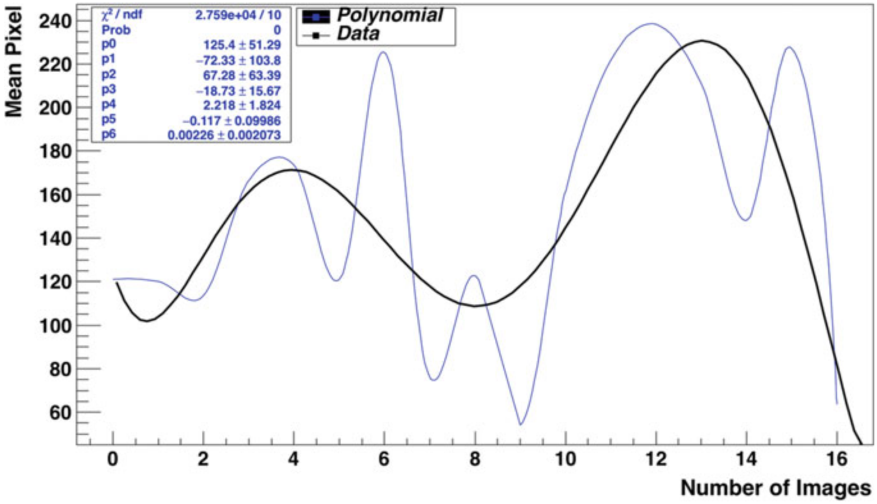

Fig. 4.53 Mean pixel of satellite images

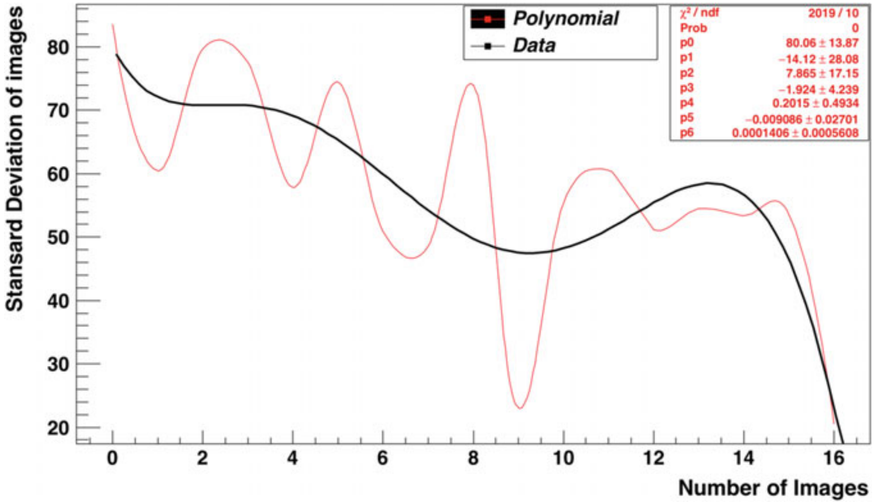

Fig. 4.54 Standard deviation of satellite images

e.g. Makefile, executable file, programme which are defined in '.cpp', '.o' and '.d' while macro makes use of smaller tools which are more easily developed as scripts.

When planning to write a program, the following rules are essential:

i. understand your application programme very well;
ii. compile or build compatible libraries for your job specification;
iii. know how to link your libraries and application. The adopted Makefile are key towards a successful link;

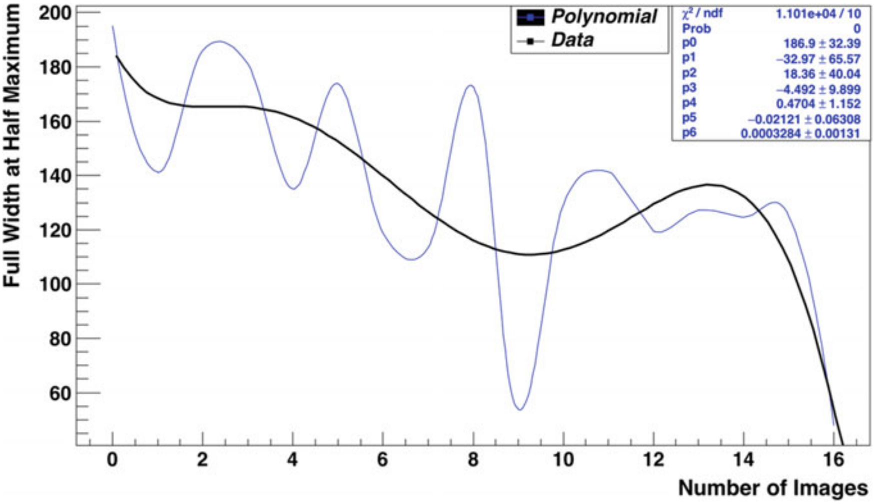

Fig. 4.55 Full width at half maximum of satellite images

iv. Choice of compiler for your platform is very essential.

For example, the program used to illustrate analysis in this book was CERN-Root and the libraries were Tiff and OpenCV. The modalities for arranging the programme are:

i. Write an appropriate header files
ii. Write the application and library linker
iii. State the global parameters
iv. State the prototypes
v. Decide on the type of main program you want. Most programmer use the argc-argv functionality
vi. Define your input, set-up and root files
vii. Choose carefully the process of uploading the input image or dataset
viii. Write your programme to your discretion

Find attached an example of codes used to process the satellite images. This process can be used to analyze more than one terabytes of data if the data has the same format.

```
//header files
#include "stdio.h"
#include "stdlib.h"
#include "TAxis.h"
#include "TH2D.h"
#include <TProfile.h>
#include "TF2.h"
#include <TF1.h>
#include "TMath.h"
#include "TCanvas.h"
#include "TStyle.h"
#include "TRandom3.h"
#include <TSystem.h>
#include "TVirtualFitter.h"
#include "TList.h"
#include <iostream>
#include "TArrayD.h"
#include <TApplication.h>
#include <TFitResult.h>
#include <fstream>
#include <TImage.h>
#include <TLegend.h>
#include <cmath>
#include <fstream>
#include <string>
#include <sstream>
#include <opencv2/core/core.hpp>
#include <opencv2/highgui/highgui.hpp>
#include <opencv2/imgproc/imgproc.hpp>
#include <algorithm>
#include <vector>
#include <stdio.h>
#include <stdlib.h>
#include <map>
#include <TApplication.h>
```

```
#include <TRoot.h>
#include <TFile.h>
#include <TNtuple.h>
#include <TASImage.h>
#include <TImage.h>
#include <TTreeReader.h>
#include <TLegendEntry.h>
#include <TCutG.h>
#include <experimental/string_view>

using namespace std;
using namespace cv;

//Library linker
R__ADD_LIBRARY_PATH (/usr/local/include/opencv2);
R__LOAD_LIBRARY(libopencv_highgui.2.4.13.dylib);
R__LOAD_LIBRARY(libopencv_core.2.4.13.dylib);

// Link to save results in ërootí file
  ofstream myfile;

// Globals
TObject *MyObj = 0;
double xfitRange1;
double xfitRange2;
double yfitRange1;
double yfitRange2;
double scale;   // height of peak
double width;   // width of peak
double bg;   // backgd
Double_t xpeak;
Double_t ypeak;

//Prototypes
```

```
TH2I* Remove_hot_pixels(TH2I* h);
void drawHist(TH2D* hist, TCanvas &c);
TF2* getFitFunction(string funcName);
Double_t get2DIntegral(TF2* fn, Double_t limit, Double_t stepSize);
Double_t gausFn(Double_t *x, Double_t *par) ;



int main(int argc, char **argv) {

  if(argc==1){
printf("Usage  : %s  <inputfile 1>   <rootfile> \n",argv[0]);
printf("Option : nothing yet \n");
exit(0);
  }

// Extract input file name 1 from the argument list
    char input_file_1[100];   // input file
    strcpy(input_file_1,argv[1]);

// Extract ROOT output file name from the argument list
    char root_file[64];   // root file
    strcpy(root_file,argv[2]);

    cout << "\n"<<input_file_1<<" and "<<root_file<<" \n\n";

    gROOT->Reset();
    TApplication*TheApp=new    TApplication("DAQanalisys",&argc,argv);
    TCanvas *MyCanvas = new TCanvas("canv", "Stuff",1200,800);
    MyCanvas->Divide(2,2);

// Make a soft link in the project directory to the data called DATA
    TString PathToData = "DATA/";
    TString input_1 = PathToData+input_file_1;
    std::cout << "Reading file  " << input_1 << endl;
```

```
    char *y = new char[input_1.Length() + 1];
    std::strcpy(y, input_1);

    cv::Mat image_in;
        cv::Mat image_out;
    image_in = cv::imread(y, CV_LOAD_IMAGE_GRAYSCALE | 
CV_LOAD_IMAGE_ANYDEPTH);   // Read the file
    delete[] y;
    if(! image_in.data ) for invalid input
    {
       cout <<  "Could not open or find the image" << std::endl ;
       return -1;
    }



    cout<<"Filling histo"<<endl;
    Double_t * argb = new Double_t [image_in.rows*image_in.cols];
    TH2I *h2 = new TH2I("h2","h2",image_in.cols,0,image_in.cols-
1,image_in.rows,0,image_in.rows-1);
    TH2I *h2_1 = new TH2I("h2_1","h2_1",image_in.cols,0,image_in.cols-
1,image_in.rows,0,image_in.rows-1);
    ushort pixel ;
    for(int i = 0; i < image_in.cols; i++)
     {
     for(int j = 0; j < image_in.rows; j++)
       {
         pixel = (ushort)image_in.at<ushort>(j, i);
         argb[i*image_in.rows+j] = pixel;
         h2->Fill(i+1,image_in.rows-j,pixel);
                    std::cout << "("<< i<<", "<<j<<") "<<"Pixels = " << pixel << endl;
       }
     }
     UInt_t yPixels = image_in.rows;
     UInt_t xPixels = image_in.cols;
```

```
    std::cout << "xPixels = " << xPixels << "  :  yPixels = " << yPixels << endl;

    gStyle->SetCanvasPreferGL(kTRUE);
    cout<<"Now plotting"<<endl;
    MyCanvas->cd(1);
    h2->SetStats(kFALSE);
    h2->Draw("lego2");
    h2_1 = Remove_hot_pixels(h2);
    MyCanvas->cd(2);
    h2_1->SetStats(kFALSE);
    h2_1->Draw("lego2");

    TH1D *h1;
    h1 = h2_1->ProjectionX();
    MyCanvas->cd(3);
    h1->Draw("HIST");
    MyCanvas->Update();
    gPad->Modified();               // make sure
    gPad->Update();                   // hist is drawn
    gSystem->ProcessEvents();

// Put errors on the Histogram to force the fit to respect the peak
    Double_t h_Max = h2_1->GetBinContent(h2_1->GetMaximumBin());
    cout <<  " Max value  " << h_Max << endl;
    for (int row=0; row<xPixels; ++row) {
      for (int col=0; col<yPixels; ++col) {
        Double_t h_bin = h2_1->GetBinContent(h2_1->GetBin(row+1,col+1));
        if( h_bin < 0.1 * h_Max){
          h2_1->SetBinError(row+1,col+1,100);
         }
        else{
         h2_1->SetBinError(row+1,col+1,sqrt(h_bin));
         }
```

```
           }
          }



          // Set the fitting parameters start value and fit range
          xpeak  =  h1->GetXaxis()->GetBinCenter(h1->GetMaximumBin());  //  x  pos  of
     peak
          h1 = h2_1->ProjectionY();
          ypeak  =  h1->GetXaxis()->GetBinCenter(h1->GetMaximumBin());  //  y  pos  of
     peak
          cout << "Peak position start values  (" << xpeak << " ,  " << ypeak <<")" <<
     endl;
          scale = 20000;   // height of peak
          width = 20;   // width of peak
          bg = 2000;   // background

          Int_t plot_range = 100;
                      Int_t a;
          TH2I *h2_2 = new
           TH2I("h2_2","h2_2",2*plot_range+1,(Int_t)xpeak-
     plot_range,(Int_t)xpeak+plot_range+1,
                         2*plot_range+1,(Int_t)ypeak-
     plot_range,(Int_t)ypeak+plot_range+1);
          for ( int i = 0; i < 2*plot_range+1; i++) {
           for ( int j = 0; j < 2*plot_range+1; j++) {
            a        =        h2_1->GetBinContent(i+(Int_t)xpeak-plot_range,j+(Int_t)ypeak-
     plot_range);
            h2_2->Fill(i+(Int_t)xpeak-plot_range,j+(Int_t)ypeak-plot_range,a);

           }
          }
          xfitRange1 = xpeak-100;
          xfitRange2 = xpeak+100;
```

```
          yfitRange1 = ypeak-100;
          yfitRange2 = ypeak+100;



// Now draw Histo over smaller range to prep for fit display
           TCutG *cutg = new TCutG("cutg",5);
           cutg->SetVarX("x");
           cutg->SetVarY("y");
           double xplotRange1 = xpeak-50;
           double xplotRange2 = xpeak+50;
           double yplotRange1 = ypeak-50;
           double yplotRange2 = ypeak+50;
           cutg->SetPoint(0,xplotRange1,yplotRange1);
           cutg->SetPoint(1,xplotRange1,yplotRange2);
           cutg->SetPoint(2,xplotRange2,yplotRange2);
           cutg->SetPoint(3,xplotRange2,yplotRange1);
           cutg->SetPoint(4,xplotRange1,yplotRange1);
           MyCanvas->cd(4);
           h2_2->Draw("surf2");
           MyCanvas->Update();
           gPad->Modified();          // make sure
           gPad->Update();             // hist is drawn
           gSystem->ProcessEvents();

//Set the fit function to be any of the above
   cout<<"getting fit function"<<endl;
   TF2* fitFunc = getFitFunction("gaus2D");
   fitFunc->SetParameters(xpeak,ypeak, scale, width,bg);
   fitFunc->SetNpx(40);
   fitFunc->SetNpy(40);

   TFitResultPtr r = h2_2->Fit(fitFunc,"SN");

   // The output .root file
```

```
   TString filename_ROOT = "root_file";
   TFile *f = new TFile(filename_ROOT,"RECREATE");

   cout << endl<<"Results of fit"<<endl;
   cout << "Peak pos :  (" << r->Parameter(0) << " ,  " << r->Parameter(1) <<")" <<
endl;
   cout << "Scale    :  (" << r->Parameter(2) << endl;
   cout << "Width    :  (" << r->Parameter(3) << endl;

   fitFunc->SetParameters(r->Parameter(0),r->Parameter(1),r->Parameter(2),r-
>Parameter(3));

   fitFunc->Draw("surf1 same bb [cutg]");
   MyCanvas->Update();
   gPad->Modified();                    // make sure
   gPad->Update();              // hist is drawn
   gSystem->ProcessEvents();
   float calibration = 1; //pixels/mm
   float units = 1.;
  cout<<"FWHM="<<2.35*r>Parameter(3)*units/calibration<<endl;
char output_file[100];
   sprintf(output_file, "%s.txt",root_file);
   myfile.open (output_file, ios::app);

   f->Write();
   std::cout << "\n Done  ...  Now waiting...";
   std::cout << "\n ==> Double click mouse button in graphics window to end
program.\n\n\n";
   int n=1;
   while (n>0) {
     MyObj = gPad->WaitPrimitive();
             if (!MyObj) break;
             printf("Loop    i=%d,    found    objIsA=%s,    name=%s\n",n,MyObj-
>ClassName(),MyObj->GetName());
```

```
            }

      myfile.close();
      delete h2;
      delete h2_1;
      delete f;

  cv::waitKey(0);                              // Wait for a keystroke in the window

  }
```

// definition of the prototypes

```
TH2I* Remove_hot_pixels(TH2I* h1) {
  Int_t ncellsx = h1->GetNbinsX();
  Int_t ncellsy = h1->GetNbinsY();
  TH2I * h2 = (TH2I*)h1->Clone("h2");
  Int_t pixel;
  Int_t pixel_av;
  Int_t pixel_1;
  Int_t pixel_2;
  Int_t pixel_3;
  Int_t pixel_4;
  Int_t n_bad_pixels = 0;
  for (int row=5; row<ncellsx-5; ++row) {
    for (int col=5; col<ncellsy-5; ++col) {
      pixel = h1->GetBinContent(h1->GetBin(row+1,col+1));
      pixel_1 = h1->GetBinContent(h1->GetBin(row+1,col));
      pixel_2 = h1->GetBinContent(h1->GetBin(row+1,col+2));
      pixel_3 = h1->GetBinContent(h1->GetBin(row,col+1));
      pixel_4 = h1->GetBinContent(h1->GetBin(row+2,col+1));
      pixel_av = (pixel_1 + pixel_2 + pixel_3 + pixel_4)/4;
      if( pixel > pixel_av + 5.0*sqrt(pixel_av) + 10 || pixel < pixel_av -
5.0*sqrt(pixel_av) - 10 ){
        n_bad_pixels++;
```

```
        //cout << "Found hot pixel at :  " << row << " , " << col << endl;
        h2->SetBinContent(h1->GetBin(row+1,col+1), pixel_av);
       }
     }
   }
   cout << "Number of bad pixels = " << (float)n_bad_pixels/( (float)ncellsx *
(float)ncellsy ) << endl;
   return h2;
}

void drawHist(TH2D* hist, TCanvas &c) {
   hist->GetXaxis()->SetTitle("X [cm]");
   hist->GetYaxis()->SetTitle("Y [cm]");
   hist->GetZaxis()->SetTitle("Grey Scale");

   hist->GetXaxis()->SetTitleOffset(1.5);
   hist->GetYaxis()->SetTitleOffset(1.5);
   hist->GetZaxis()->SetTitleOffset(1.5);

   string name = hist->GetName();
   name += "c";
   c.cd();

   hist->Draw("lego2");
   c.Update();

}

Double_t gausFn(Double_t *x, Double_t *par) {
   Double_t xv = x[0] - par[0];
   Double_t yv = x[1] - par[1];
   Double_t r = TMath::Sqrt(xv * xv + yv * yv);
   return par[2] * TMath::Gaus(r, 0, par[3])+par[4];
}
```

```
TF2* getFitFunction(string funcName) {
   TF2* fitFunc = nullptr;

   if (funcName == "gaus2D") {
      fitFunc = new TF2("gaus2D", gausFn, xfitRange1, xfitRange2, yfitRange1,
yfitRange2, 5);
      fitFunc->SetParName(0, "x pos");
      fitFunc->SetParName(1, "y pos");
      fitFunc->SetParName(2, "scale");
      fitFunc->SetParName(3, "Sigma");
      fitFunc->SetParName(4, "backgd");
   }

   return fitFunc;
}


Double_t get2DIntegral(TF2* fn, Double_t limit, Double_t stepSize) {
   double integral = 0;
   for (double x = -limit; x < limit; x += stepSize) {
      for (double y = -limit; y < limit; y += stepSize) {
         if (x * x + y * y > limit) continue;
         integral += fn->Eval(x, y);
      }
   }
   return integral * (stepSize * stepSize);
}
```

The beauty of writing a compiled program is that results or outputs can be stored in predefined folders. The output files or images can be saved with their original file names or titles. Hence, it is easier to work with volume of data that is above one terabytes. Depending on the body of the program, it is interesting to note that the execution time is impressive. This means that a very fast computer may not be used to work on ‘big data’ as earlier proposed. The definition and scope of ‘big data’ in environmental science will be discussed in chapter five.

In writing macro, the library may be linked to the main program statically. Much header file may not be defined as in a program. Global parameters are defined within the ‘void’ or ‘main’ prototype. Find attach an example of a macro written to analyze large volume of dataset.

```
//Header file
#include "opencv2/highgui/highgui.hpp"
#include "opencv2/imgproc/imgproc.hpp"
#include <iostream>
#include <stdio.h>
#include <fstream>
using namespace std;
using namespace cv;

//Globals
Mat src, dst, des;

//prototype
char window_name[20]="Pixel Value Demo";

int main( int argc, char** argv )
{


   /// Load image from folder

   vector<String> filenames;

   string folder = "/Users/emetere/Desktop/processed/*.tif";
   cv::glob(folder, filenames);
```

```
  for(size_t i = 0; i < filenames.size(); ++i)
  {
    cv::Mat3b const src = imread(filenames[i], cv::IMREAD_COLOR);

    if( !src.data )
    { return -1; }

    /// Separate the image in 3 places ( B, G and R )
    vector<Mat> bgr_planes;
    split( src, bgr_planes );

    /// Establish the number of bins
    int histSize = 256;

    /// Set the ranges ( for B,G,R) )
    float range[] = { 0, 256 } ;
    const float* histRange = { range };

    bool uniform = true; bool accumulate = false;

    Mat b_hist, g_hist, r_hist;

    /// Compute the histograms:
    calcHist( &bgr_planes[0], 1, 0, Mat(), b_hist, 1, &histSize, &histRange, uniform,
accumulate );
    calcHist( &bgr_planes[1], 1, 0, Mat(), g_hist, 1, &histSize, &histRange, uniform,
accumulate );
    calcHist( &bgr_planes[2], 1, 0, Mat(), r_hist, 1, &histSize, &histRange, uniform,
accumulate );

    // Draw the histograms for B, G and R
    int hist_w = 512; int hist_h = 400;
    int bin_w = cvRound( (double) hist_w/histSize );
```

```
Mat histImage( hist_h, hist_w, CV_8UC3, Scalar( 255,255,255) );

/// Normalize the result to [ 0, histImage.rows ]
normalize(b_hist, b_hist, 0, histImage.rows, NORM_MINMAX, -1, Mat() );
normalize(g_hist, g_hist, 0, histImage.rows, NORM_MINMAX, -1, Mat() );
normalize(r_hist, r_hist, 0, histImage.rows, NORM_MINMAX, -1, Mat() );

/// Draw for each channel
for( int i = 1; i < histSize; i++ )
{
   line( histImage, Point( bin_w*(i-1), hist_h - cvRound(b_hist.at<float>(i-1)) ) ,
       Point( bin_w*(i), hist_h - cvRound(b_hist.at<float>(i)) ),
       Scalar( 255, 0, 0), 2, 8, 0 );
   line( histImage, Point( bin_w*(i-1), hist_h - cvRound(g_hist.at<float>(i-1)) ) ,
       Point( bin_w*(i), hist_h - cvRound(g_hist.at<float>(i)) ),
       Scalar( 0, 255, 0), 2, 8, 0 );
   line( histImage, Point( bin_w*(i-1), hist_h - cvRound(r_hist.at<float>(i-1)) ) ,
       Point( bin_w*(i), hist_h - cvRound(r_hist.at<float>(i)) ),
       Scalar( 0, 0, 255), 2, 8, 0  );
}

/// Display
namedWindow("calcHist Demo", CV_WINDOW_AUTOSIZE );
imshow("calcHist Demo", histImage );
histImage.convertTo(dst, CV_8UC3);
std::ostringstream name;
name   <<   "/Users/emetere/Desktop/intensity/jpg/Phi-1to4speed0.01_2017-10-
21-201727-0" << i << ".jpg";
cv::imwrite(name.str(),dst);

///Saving into text
   int j, k;
   std::ofstream pfout("/Users/emetere/Desktop/intensity/output_test.txt");
   Vec3b pix=src.at<Vec3b>(k,j);
```

```
        int Red=src.at<cv::Vec3b>(k,j)[2];
        int Green= src.at<cv::Vec3b>(k,j)[1];
        int Blue = src.at<cv::Vec3b>(k,j)[0];
        int y= src.at<cv::Vec3b>(k,j)[3];
        int x = src.at<cv::Vec3b>(k,j)[4];
        int Totalintensity = 0;
        for (int u=0; u < src.rows; ++u){
        for (int v=0; v < src.cols; ++v){
          Totalintensity += (int)src.at<uchar>(u, v);
            }
          }

        // Find avg lum of frame
        float avgLum = 0;
        avgLum = Totalintensity/(src.rows * src.cols);

        cout<<"   x= "<<x<<"   y= "<<y<<"   Red= "<<Red<<"   Green=   "<<Green<<"
 Blue= "<<Blue<<"  intensity of images = "<<avgLum<<" \t\n";
        pfout<<"   x= "<<x<<"   y= "<<y<<"   Red= "<<Red<<"   Green=   "<<Green<<"
 Blue= "<<Blue<<"  intensity of images = "<<avgLum<<" \t\n";

      ///geting axis
      Vec3f intensity = src.at<Vec3f>(y, x);
      float blue = intensity.val[0];
      float green = intensity.val[1];
      float red = intensity.val[2];
      pfout<<"  Red= "<<red<<"  Green=  "<<green<<"  Blue= "<<blue<<" \t\n";
      cout<<"  Red= "<<red<<"  Green=  "<<green<<"  Blue= "<<blue<<" \t\n";

      ///plot function
      Mat plot_result;

    }
    waitKey(0);
      return 0;
    }
```

4.4 Planning a Computational and Mathematical Model Design Insights into 'Big Data' Analysis

Planning a computational or Mathematical Model large volumes of dataset of images require the following skill:

i. an in-depth understanding of a code to extract required information from the image;
ii. quantifying the information to numbers;
iii. understand the theoretical background of quantified information;
iv. be able to manipulate the information to suite your research objectives.

These skills are essential to dig-out unimaginable information from an image and apply it to a very large dataset (i.e. big data) of images of same kind. The main objective of this section is to show how to generate a computational model from a large dataset of images.

In this illustration, 1568 images of a dataset were analyzed. The matrix of each images were categorized into column (y-axis) pixels and row (x-axis) pixels. Based on the listed information, it is possible to expand or manipulate numerical information extracted from the dataset. In Fig. 4.56a, b, the mean-intensity of the images was extracted. The polynomial of the trend is shown at the top-left corner of the figure. The values of the polynomial trend may be used to develop a mathematical model. However, the focus is to show how computational model can be developed from large dataset. Hence, the steps that shall be considered in the computational model are:

i. give a 2D-plot of the images in sequential order. In this book, the mean-pixel of each images were considered;
ii. choose the significant spots of interest. This process specifies on unique information that may be indicated as new or existing concept;
iii. do the 3D-plot of each spot;
iv. do a Gaussian fit for each spot to know if they all have same set of principle;
v. consider more parameters with emphasis on the spot analysis;
vi. draw out your conclusion on the spot analysis.

It is observed from Fig. 4.56a, b that significant perturbation of the linearity of the graph was at 550, 750, 825, 910, 1020, 1100 and 1125. This means that the information on these spots may refer to the already known principle or may refer to a new event. The easiest way of knowing if information exists or is a new concept is your familiarity to the literature of the subject-matter. The spot analysis was done using a 3D image as in Fig. 4.57. To understand the significant changes that has occurred in each spot, a spot will be taken from the linear or uniform trend of the graph. Hence, Fig. 4.57a is the normal spot and Fig. 4.57b-h refers to the highlighted spots listed above (i.e. 550, 750, 825, 910, 1020, 1100 and 1125).

As mentioned above, the relevance of the spot analysis is to critically examine if a new result has been found or an existing result has been validated. For example, the Gwydion software was used to analyze the satellite map as shown below.

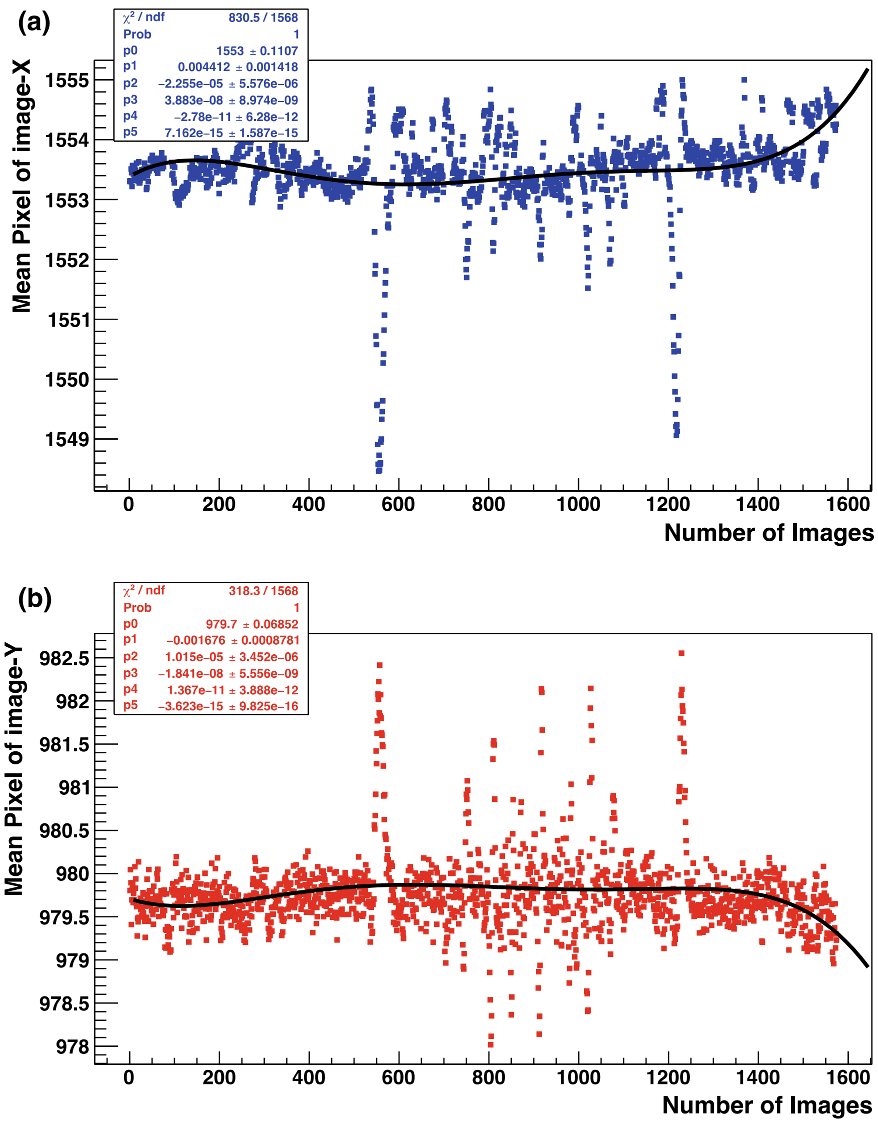

Fig. 4.56 Mean pixel of images. **a** Pixel in the column-imageY, **b** pixel in the row-imageX

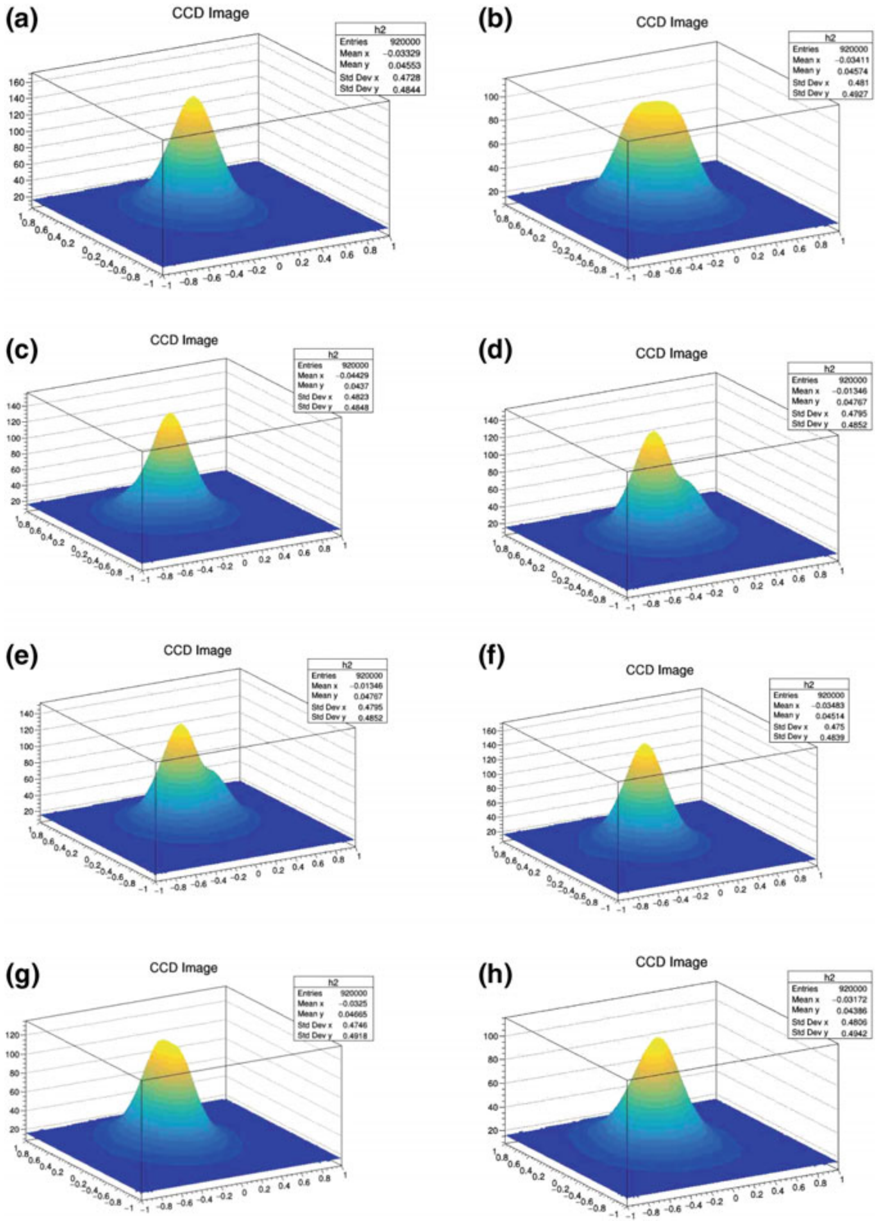

Fig. 4.57 The 3D-plot for each spot. **a** Normal spot, **b** 550, **c** 750, **d** 825, **e** 910, **f** 1020, **g** 1100, **h** 1125

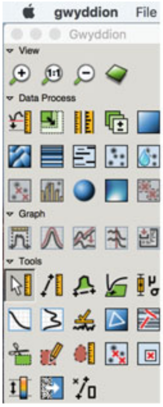

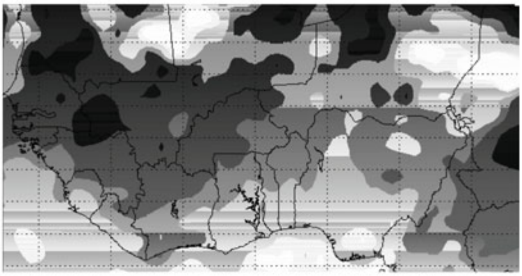

The above image can be used to design specific objects in 2D as shown below. It is interesting that the 2D image can be further processed as a whole (as shown below) or individually processed as shown in Fig. 4.57. Each of the points can be further separated either by snapping areas of interest the use of crop tools. It was observed that the analysis of each spot is not the same when further processed as shown in Fig. 4.57. This process is tedious, however, through the use of openCV, it is possible to analyze large dataset without much stress.

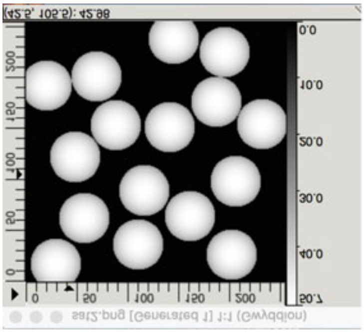

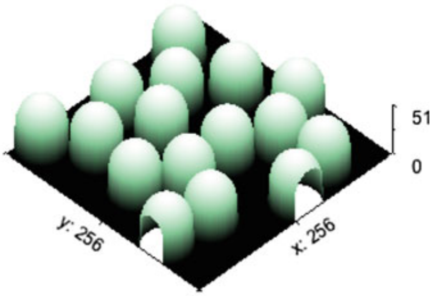

Taking a keen look at the 3D-plot (i.e. comparing Fig. 4.57b–h with Fig. 4.57a), it was observed that at the 555th image, the peak is flat and broadened (Fig. 4.57b). Further interpretation depends on the readers' familiarity with literature. There is an elongation on the left-hand side of the peak in the 750th image (Fig. 4.57c). In practical terms, there must be a significant transition from Fig. 4.57b, c. The quantification of the transition can be done by considering the x-projection and y-projections of both graphs. Recall the mathematical significance of the x- and y-projections has been discussed in the early part of this chapter. Figure 4.57d, e show the event in the spot-analysis of the 825th and 910th images. Both images have a deformed and elongated right-hand side of the peak. This certainly means that the same set of event occurred on each spot.

Figure 4.57f show a significant deformation at the base of the peak. This means that there is a significant event between the 910th and 1020th image. Aside the use of the x- and y-projections, a code that calculates the difference between the pixels of each image can be written as shown below in Sect. 4.4.1. Figure 4.57g show a flattened peak i.e. similar to Fig. 4.57b. Hence, the 555th may have same event as the 1100th image.

Figure 4.57h has a significant broadening at the base of the peak and a very narrow peak at the top. This event is almost similar to Fig. 4.57f. In general, the spot analysis reveal that events can alternatively occur within the confine of same experiment. Hence the next step was to apply the Gaussian fit as shown in Fig. 4.58a–h. It is observed that Gaussian fit for Fig. 4.58g was not appropriate. Hence, the need to further statistically investigate the whole images by looking at the kurtosis (Fig. 4.59a, b), deviation error (Fig. 4.60a, b) and skew (Fig. 4.61a, b).

The surface appearance of Fig. 4.59a, b may look somewhat similar but a keen or closer observation shows that there are significant differences between both images. First, the polynomial factors in both images differ. Second, there are additional spots over the main curve in Fig. 4.59b. So what does this signify? The interpretation of the Fig. 4.59 should be related to the statistical significance of kurtosis. Kutosis is defined as a measure of the "tailedness" of the probability distribution of a real-valued random variable. It is a descriptor of the shape of a probability distribution. Hence, kurtosis can be interpreted based on the following:

i. scaled version of the fourth moment of the dataset;
ii. the type of kurtosis distribution i.e. mesokurtic, leptokurtic and leptokurtic;
iii. scaled version of the fourth L-moment.

The details of kurtosis can be obtained from most statistical textbooks. The distribution of Fig. 4.59a, b is referred to as platykurtic distribution because its distribution is less than 3. These types of distributions have slender tails, broad-looking peak and a peak that is smaller than a mesokurtic distribution.

Figure 4.60a, b describes the deviation error within the images. The trends of Fig. 4.60 are more similar than Fig. 4.59. However, there are differences looking at the values of the polynomial factors that is located at the top-left corner of the graph. Secondly, the mean pixel along the y-axis of the images (Fig. 4.60a) is lower than the mean pixel along the x-axis (Fig. 4.60b). This shows that there are major changes along the column or latitude of the images. Like the kurtosis, the interpretation of Fig. 4.60 is based on the statistical definition of deviation error. Deviation error or standard error of the dataset is defined as the standard deviation of its sampling distribution. Reader should note that there is a difference between standard deviation and deviation/standard error. Standard deviation is a measure of dispersion of the data from the mean while deviation error is a measure of how precise is the estimate of the mean. In general, the deviation in Fig. 4.60 shows how similar the images are.

Figure 4.61a, b differ from Figs. 4.59 and 4.60 because the skewness of image-X is significantly different from the skew of image-Y. This shows that the skewness of the image pixels on the column and rows gives different information. The question is what is skewness? Skewness is defined as the measure of the asymmetry of the probability

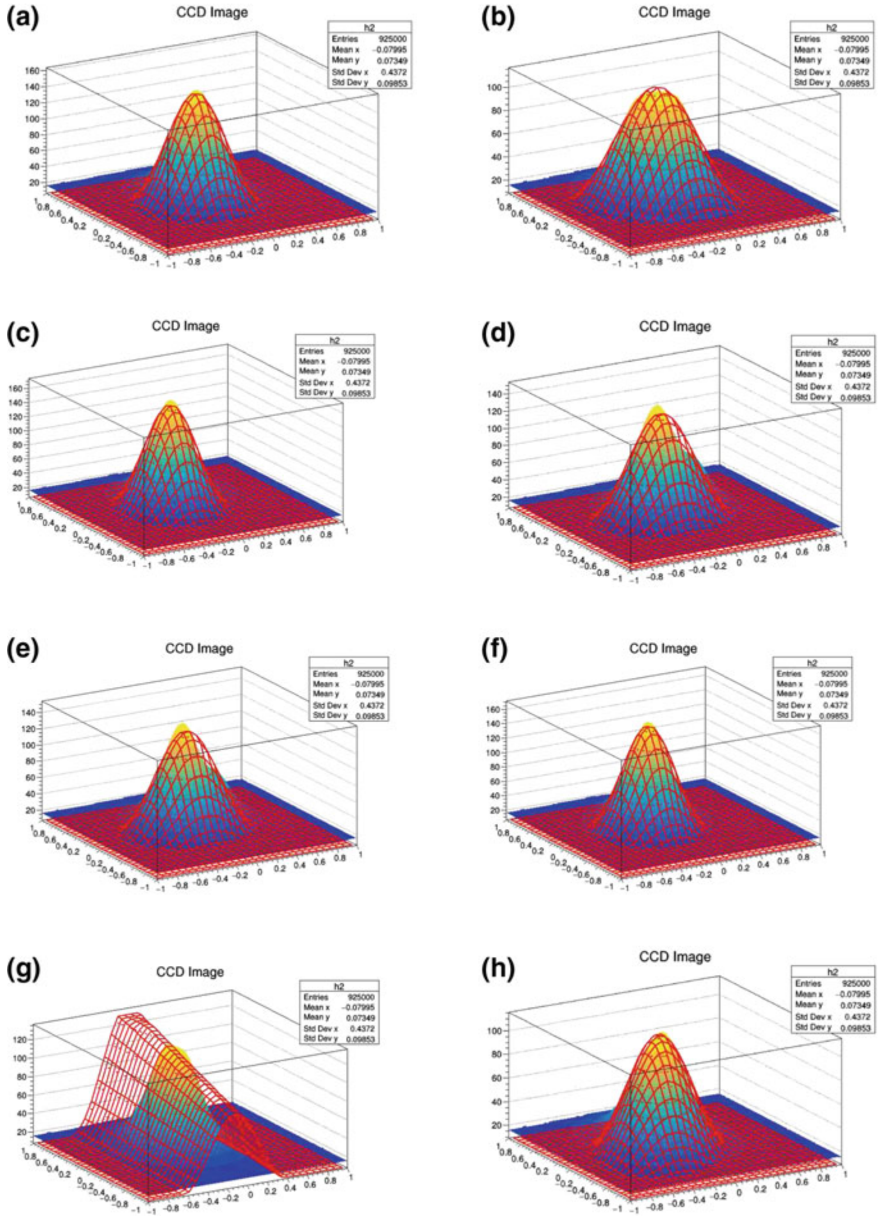

Fig. 4.58 The Gaussian fit for each spot. **a** Normal spot, **b** 550, **c** 750, **d** 825, **e** 910, **f** 1020, **g** 1100, **h** 1125

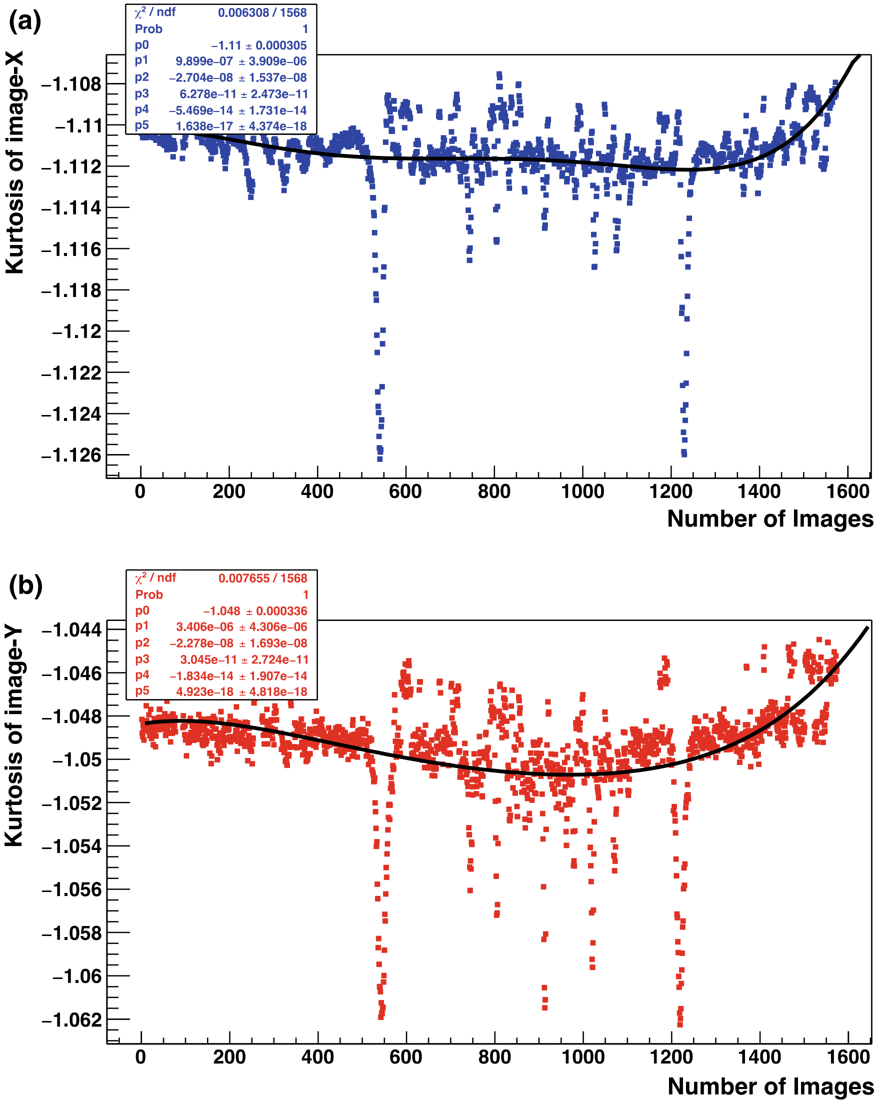

Fig. 4.59 Kurtosis of images. **a** Pixel in the column—imageY. **b** Pixel in the row—imageX

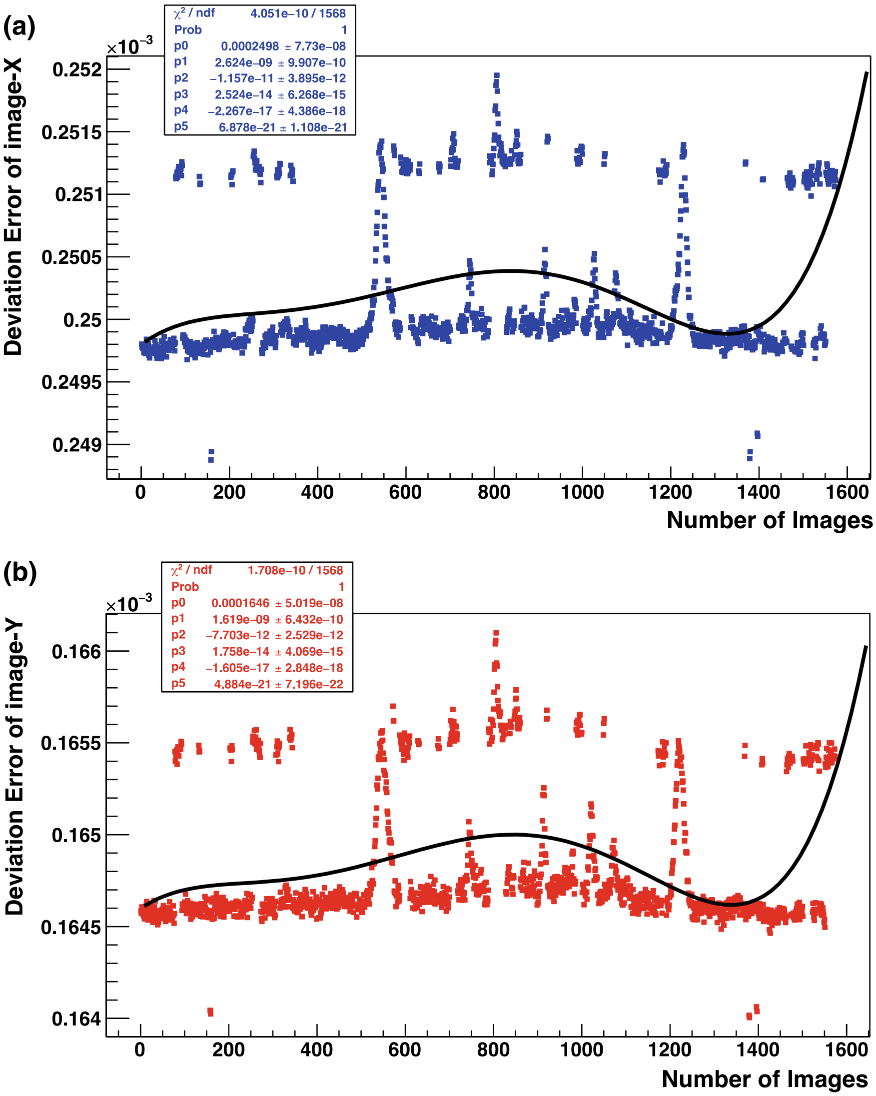

Fig. 4.60 Deviation error of images. **a** Pixel in the column—imageY. **b** Pixel in the row—imageX

distribution of a real-valued random variable about its mean. The Pearson's first coefficient is the skewness of the dataset. It is measured by subtracting the mean from the mode, and then divide the difference by the standard deviation of the data. Unlike kurtosis, the qualitative interpretation of the skew is complicated and unintuitive. With respect to Fig. 4.61, the positive skew (right-skew) indicates that the tail on the right side is longer or fatter than the left side while the negative skew (left-skew) indicates a long tail in the negative direction on the number line.

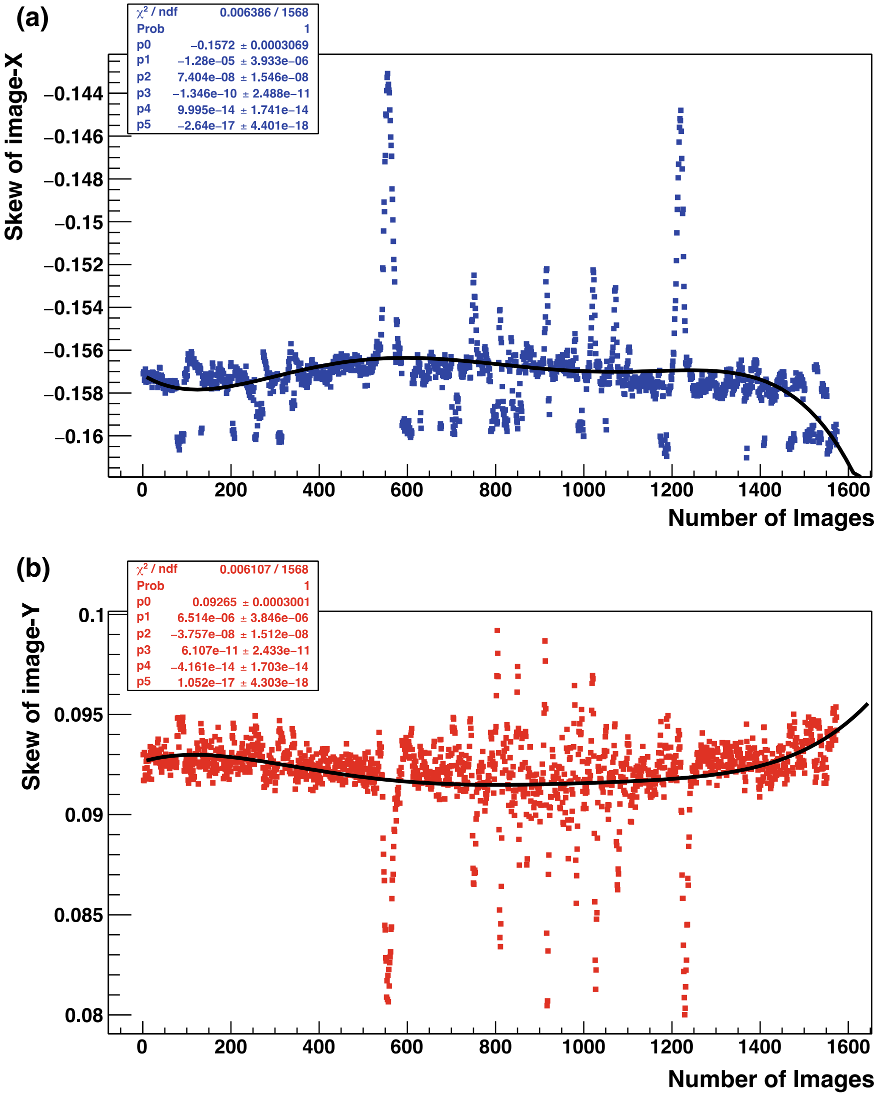

Fig. 4.61 Skew of images. **a** Pixel in the column—imageY. **b** Pixel in the row—imageX

The second part of this section is the development of a mathematical model. Let us assume a general polynomial for the trend of the images as:

$$z_x = p_5x^5 + p_4x^4 + p_3x^3 + p_2x^2 + p_1x + p_0 \tag{4.5}$$

$$z_y = p_5y^5 + p_4y^4 + p_3y^3 + p_2y^2 + p_1y + p_0 \tag{4.6}$$

Here z_x the pixel of image-X, z_y is the pixel of image-Y, x and y represents the individual components of the pixel in x- and y-axis. The third dimension is the introduction of image resolution (z_z).

$$z_z = \frac{\text{Number of pixel (z)}}{\text{Field of view (fov)}} \tag{4.7}$$

if the z is written as:

$$z = \sum x \times \sum y = \sum yx \tag{4.8}$$

$$z_z = \frac{1}{\text{fov}} \sum yx \approx \frac{1}{\text{fov}} xy \tag{4.9}$$

$$\text{fov} = \alpha \frac{D}{d} \tag{4.10}$$

where D is dimension of full image (xy), d is the dimension of target (≈1), α is the targets angular extent (≈1). The target parameters were set to unity since no target was considered.

If Eqs. 4.5, 4.6 and 4.9 are differentiated with respect to time (t).

$$\frac{dz_x}{dt} = vp_5x^4 + vp_4x^3 + vp_3x^2 + vp_2x + vp_1 \tag{4.11}$$

$$\frac{dz_y}{dt} = \vartheta p_5y^4 + \vartheta p_4y^3 + \vartheta p_3y^2 + \vartheta p_2y + \vartheta p_1 \tag{4.12}$$

$$\frac{dz_z}{dt} = \vartheta xz \tag{4.13}$$

here $v = \frac{dx}{dt}$ and $\vartheta = \frac{dy}{dt}$.

Then z must be introduced to Eqs. 4.11 and 4.12. Thus multiply Eq. 4.11 by y and Eq. 4.12 by x.

$$y\frac{dz_x}{dt} = yvp_5x^4 + yvp_4x^3 + yvp_3x^2 + yvp_2x + yvp_1 \tag{4.14}$$

$$x\frac{dz_y}{dt} = x\vartheta p_5y^4 + x\vartheta p_4y^3 + x\vartheta p_3y^2 + x\vartheta p_2y + x\vartheta p_1 \tag{4.15}$$

$$\frac{dz_z}{dt} = \vartheta xz \tag{4.16}$$

Assume that $x^nx^m = 0$

$$y\frac{dz_x}{dt} = vp_2z + vp_1y \tag{4.17}$$

Table 4.2 Numerical solutions of governing equations

t	z_x	z_y	z_z
0	10	1	1
0.1	10	0.999997	1.0202
0.55	10	0.999981	1.11628
1.9242	10.0002	0.999935	1.46938
3.29839	10.0004	0.999889	1.93419
4.67259	10.0006	0.999843	2.54605
6.04679	10.0009	0.999797	3.35148
7.42098	10.0013	0.999751	4.41175
8.79518	10.0019	0.999706	5.80752
10.1694	10.0026	0.999661	7.64502
11.5436	10.0035	0.999617	10.0641
12.9178	10.0048	0.999573	13.2491
14.292	10.0065	0.999531	17.4428
15.6662	10.0086	0.999489	22.965
17.0404	10.0115	0.99945	30.2376
18.4146	10.0153	0.999413	39.8168
19.7888	10.0203	0.999379	52.4371
21.163	10.0268	0.999349	69.0684
22.5371	10.0355	0.999324	90.9935
23.9113	10.0469	0.999306	119.911
25.2855	10.0619	0.999297	158.076
26.6597	10.0817	0.999301	208.487
28.0339	10.1079	0.99932	275.148
29.4081	10.1424	0.99936	363.422
30.7823	10.188	0.999429	480.542
32.0039	10.2408	0.999521	616.737
33.2255	10.3086	0.999651	792.692
34.4471	10.3959	0.999829	1020.77
35.6686	10.5083	1.00007	1317.66
36.8902	10.6538	1.0004	1706.24
38.1118	10.8425	1.00083	2218.4
39.3334	11.0884	1.00141	2899.54
40.382	11.3598	1.00206	3668.74
41.4307	11.7043	1.0029	4671.92
42.4794	12.1448	1.00397	5998.29
43.408	12.6404	1.00519	7549.29
44.3366	13.2674	1.00674	9600.36
45	13.8196	1.00812	11489.1

$$x\frac{\mathrm{dz_y}}{dt} = \vartheta \mathrm{p_2 z} + \vartheta \mathrm{p_1} x \tag{4.18}$$

$$\frac{\mathrm{dz_z}}{dt} = \vartheta \mathrm{xz} \tag{4.19}$$

Hence, the three governing equations are 4.17, 4.18 and 4.19. The governing equation was solved using the numerical analysis of C++ Odeint library that can be obtained at Odient (2018). Odeint is a modern C++ library for numerically solving Ordinary Differential Equations. The solution of Eqs. 4.17–4.19 when $\vartheta = 0.02$, v = 0.018, t = 45 s is given in Table 4.2. While the resolution ($\mathrm{z_z}$) of the images is expected to increase significantly in 45 s, The values of the mean pixel increases at the x-axis at higher ratio than the mean pixel of the image at the y-axis. What is the significance of this result? The selected spots (i.e. 550, 750, 825, 910, 1020, 1100 and 1125) are spot of highest resolution. Within the high resolution (i.e. spots) the value for image-X is expected to be higher than image-Y. These results are validated by Figs. 4.56, 4.59, 4.60 and 4.61 were the values of image-X is always higher than image-Y.

Therefore, the mathematical model has exhibited high sensitivity to be used to test other results.

4.5 Macro to Determine the Difference of Images by Pixel

The code to determine the difference between two images—based on its pixel content can be itemized as:

i. write the header files
ii. state the main program header
iii. load the images
iv. resize both images to have same dimensions
v. define the height and width
vi. find the pixels along the height and width
vii. calculate the percentage change between the images

The code is written in C++, however, the reader can use any familiar computer language to write the same code.

```
#include "opencv2/highgui/highgui.hpp"
#include "opencv2/imgproc/imgproc.hpp"
#include "opencv2/core/core.hpp"
#include <iostream>
#include <algorithm>
#include <vector>
#include <stdio.h>
#include <stdlib.h>
#include <fstream>

using namespace cv;
using namespace std;



int main(){

   auto firstImage =
imread("/Users/emetere/Desktop/satellite/sat001.png",CV_LOAD_IMAGE_ANYCOL
OR);
   auto secondImage = imread("/Users/emetere/Desktop/ satellite/sat002.png
",CV_LOAD_IMAGE_ANYCOLOR);
  cv::resize(secondImage, secondImage, firstImage.size());

   if (firstImage.size()==secondImage.size())
   {
      double totaldiff = 0.0 ; //holds the number of different pixels
      int h = firstImage.size().width;
      int w = firstImage.size().height;
      int hsecond = secondImage.size().height;
      int wsecond = secondImage.size().width;
      if ( w != wsecond || h != hsecond ) {
         std::cerr << "Error, pictures must have identical dimensions!\n" ;
         return 2 ;
      }

      for ( int y = 0 ; y < h ; y++ ) {
         uint *firstLine = ( uint* )firstImage.ptr<uchar>(y) ;
         uint *secondLine = ( uint* )secondImage.ptr<uchar>(y) ;
         for ( int x = 0 ; x < w ; x++ ) {
            uint pixelFirst = firstLine[ x ] ;
            double rFirst = ((double) cv::countNonZero(pixelFirst));
            double gFirst = ((double) cv::countNonZero(pixelFirst));
            double bFirst = ((double) cv::countNonZero(pixelFirst));
            //cout<<rFirst<<" "<<gFirst<<" "<<bFirst<<" "<<endl;
```

```
                    uint pixelSecond = secondLine[ x ] ;
                    double rSecond = ((double) cv::countNonZero(pixelSecond ));
                    double gSecond = ((double) cv::countNonZero(pixelSecond ));
                    double bSecond = ((double) cv::countNonZero(pixelSecond ));
                    totaldiff += std::abs( rFirst - rSecond ) / 255.0 ;
                    totaldiff += std::abs( gFirst - gSecond ) / 255.0 ;
                    totaldiff += std::abs( bFirst -bSecond ) / 255.0 ;

              }
           }
           std::cout << "The difference of the two pictures is " <<
           (totaldiff * 100)  / (w * h * 3)  << " % !\n" ;
        }
        else
        {
           cout<<"The dimension is wrong"<<endl;
        }

        waitKey(0);
        return 0;
     }
```

References

Acker, J. G., & Leptoukh, G. (2007). Online analysis enhances use of NASA earth science data. *EOS, 88,* 14–17.

Bond, T. C., & Bergstrom, R. W. (2006). Light absorption by carbonaceous particles: an investigative review. *Aerosol Science and Technology, 40,* 27–67.

Bond, T. C., Doherty, S. J., Fahey, D. W., Forster, P. M., Berntsen, T., DeAngelo, B. J., et al. (2013). Bounding the role of black carbon in the climate system: A scientific assessment. *Journal of Geophysical Research, 118*(11), 5380–5552.

Campbell, J. B. (2002). *Introduction to remote sensing*. New York London: The Guilford Press.

Emetere, M. E. (2016a). Statistical examination of the aerosols loading over Mubi-Nigeria: The satellite observation analysis. *Geographica Panonica, 20*(1), 42–50.

Emetere, M. E. (2016b). *Numerical modelling of West Africa regional scale aerosol dispersion*. Thesis submitted to Covenant University.

Emetere, M. E. (2017). Investigations on aerosols transport over micro- and macro-scale settings of West Africa. *Environ. Eng. Res., 22*(1), 75–86.

Emetere, M. E., & Akinyemi, M. L. (2017). Documentation of atmospheric constants over Niamey, Niger: a theoretical aid for measuring instruments. *Meteorological Applications, 24*(2), 260–267.

Emetere, M. E., Akinyemi, M. L., & Akinojo, O. (2015a). Parametric retrieval model for estimating aerosol size distribution via the AERONET, LAGOS station. *Environmental Pollution, 207*(C), 381–390.

Emetere, M. E., Akinyemi, M. L., & Akin-Ojo, O. (2015b). Aerosol optical depth pollution in selected areas trends over different regions of Nigeria: Thirteen years analysis. *Modern Applied Science., 9*(9), 267–279.

Emetere, M. E., Esisio, F., Oladapo, F. (2017b). Satellite observation analysis of aerosols loading effect over Monrovia-Liberia. *Journal of Physics*: *Conference Series*, *852*(1), art. no. 012009. DOI: 10.1088/1742-6596/852/1/012009.

Emetere, M. E., Sanni, S. E., Emetere, J. M., & Uno, U. E. (2017a). Thermal Infrared remote sensing of hydrocarbon in Lagos-Southern Nigeria: Application of the thermographic model. *International Geomate Journal, 13*(39), 33–45.

Emetere, M. E., Sanni, S. E., & Tunji-Olayeni, P. (2017b). Atmospheric configurations of aerosols loading and retention over Bolgatanga-Ghana. *Journal of Physics: Conference Series, 852*(1), art. no. 012007. DOI: 10.1088/1742-6596/852/1/012007.

GeoEye. (2018). *GeoEye-1 satellite sensor (0.46 m)*. https://www.satimagingcorp.com/satellite-sensors/geoeye-1/. Accessed January 12, 2018.

Koike, M., Moteki, N., Khatri, P., Takamura, T., Takegawa, N., Kondo, Y., et al. (2014). Case study of absorption aerosol optical depth closure of black carbon over the East China Sea. *Journal of Geophysical Research, 119*(1), 122–136.

Lacis, A. A., & Mishchenko, M. I. (1995). Climate forcing, climate sensitivity, and climate response: A radiative modeling perspective on atmospheric aerosols. In R. Charlson & J. Heintzenberg (Eds.), *Aerosol forcing of climate* (pp. 11–42). New York: John Wiley.

Landinfo. (2018). *Satellite imagery resolution comparison*. http://www.landinfo.com/GalSatResComp.htm. Accessed January 12, 2018.

Lindén, J., Thorsson, S., Boman, R., Holmer, B. (2012). *Urban climate and air pollution in Ouagadougou, Burkina Faso: An overview of results from five field studies* (pp. 1–88). University of Gothenburg. http://hdl.handle.net/2077/34289.

NASA. (2015). *NASA satellite camera provides "EPIC" view of earth*. https://www.nasa.gov/press-release/nasa-satellite-camera-provides-epic-view-of-earth. Accessed January 4, 2018.

Odient. (2018). Odeint solving ODE's in C++. http://headmyshoulder.github.io/odeint-v2/. Accessed February 17, 2018.

Omotosho, T. V., Emetere, M. E., & Arase, O. S. (2015). Mathematical projections of air pollutants effects over Niger Delta region using remotely sensed satellite data. *International Journal of Applied Environmental Sciences, 10*(2), 651–664.

Rafferty, J.P. (2010). *Storms, violent winds, and earth's atmosphere*. The Rosen Publishing Group (p. 95). SBN-13: 978-1615301140, ISBN-10: 1615301143.

Senghor, H., Machu, É., Hourdin, F., Gaye, A. T. (2017). Seasonal cycle of desert aerosols in western Africa: analysis of the coastal transition with passive and active sensors. *Atmospheric Chemistry and Physics, 17*, 8395–8410.

Tegen, I., Peter, H., Mian, C., Fung, I., Jacob, D, Penn, J. (1997). Contribution of different aerosol species to the global aerosol extinction optical thickness: Estimates from model results. *Journal of Geophysical Research, 102*(D20), 23895–23915.

Tirabassi, T., Moreira, D. M., Vilhena, M. T., da Costa, C. P. (2010). Comparison between Non-Gaussian puff model and a model based on a time-dependent solution of advection-diffusion equation. *Journal of Environmental Protection, 1*, 172–178.

Walcek, C.J. (2004). *A Gaussian dispersion/plume model explicitly accounting for wind shear*. https://ams.confex.com/ams/pdfpapers/79742.pdf. Accessed January 9, 2018.